Chemical Geology 700 (2026) 123173

Contents lists available at ScienceDirect

Chemical Geology

journal homepage: www.elsevier.com/locate/chemgeo

Research Paper

Redox evolution of carbon- and sulphur-bearing clinopyroxenites as proxies of deeply recycled crustal material

Nadia Malaspina [a,*], Falko Langenhorst [b,c,d], Kilian Pollok [b,c], Valerio Cerantola [a], Mara Murri [e], Carolina Longa [a], Danilo Bersani [f], Alessandra Montanini [g]

[a] Department of Earth and Environmental Sciences, University of Milano-Bicocca, Piazza della Scienza 4, 20126 Milano, Italy
[b] Institute of Geosciences, Friedrich Schiller University Jena, Burgweg 11, 07749 Jena, Germany
[c] Center for Energy and Environmental Chemistry Jena (CEEC II Jena), Friedrich Schiller University Jena, Lessingstr. 12-14, 07743 Jena, Germany
[d] Hawai'i Institute of Geophysics and Planetology, School of Ocean and Earth Science and Technology, University of Hawai'i at Manoa, Honolulu, HI 96822, USA
[e] Department of Earth and Environmental Sciences, University of Pavia, Pavia, Italy
[f] Department of Mathematics, Physics and e Informatics Sciences, University of Parma, Parco Area delle Scienze 7/A, 43124 Parma, Italy
[g] Department of Chemistry, Life Sciences and Environmental Sustainability, University of Parma, Parco Area delle Scienze 157a, 43100 Parma, Italy

ARTICLE INFO

Editor: Sonja Aulbach

Keywords:
Off-craton pyroxenites
Oxygen fugacity
Carbon and Sulphur recycling
Synchrotron Mössbauer Spectroscopy
Electron Energy loss Spectroscopy

ABSTRACT

Fossil subduction zones are key to studying the deep geochemical cycles of C, O, and S. We analysed graphite-sulphide-bearing garnet clinopyroxenites from the External Ligurian (Northern Apennines, Italy), which serve as indicators of deep recycling of subducted crust. These rocks are among the only three known pyroxenite occurrences worldwide (along with Beni Bousera, Morocco, and Ronda, Spain) that formed through the crystallisation of eclogite-derived melts ($P \geq 3$ GPa and 1100 °C), following a prolonged recycling history in off-craton mantle. In particular, a MOR-type heterogeneous gabbroic sequence was recycled into the mantle as eclogite 1.5–1.0 Ga ago, then partially melted and crystallised in the convective mantle, followed by subsolidus re-equilibration and exhumation. We analysed the redox state of garnets and clinopyroxenes associated with graphite and sulphides in garnet clinopyroxenites, that crystallised from a liquid produced by partial melting of recycled eclogite. Electron Energy Loss Spectroscopy within a transmission electron microscope and Synchrotron micro-Mössbauer analyses revealed heterogeneities in Fe^{3+}/Fe^{2+} distribution and its partitioning among mineral phases ($Fe^{3+}/\Sigma Fe$ error is 0.03 for Electron Energy Loss Spectroscopy and 0.01–0.03 for Synchrotron micro-Mössbauer).

The analysed clinopyroxenites display three generations of clinopyroxenes: unexsolved crystals included in garnet cores with $Fe^{3+}/\Sigma Fe$ = 0.16–0.38 (representative of eclogite-derived melt crystallisation in the asthenosphere), clinoenstatite exsolution-bearing grains with $Fe^{3+}/\Sigma Fe$ = 0.03–0.10 (related to a first stage of exhumation in the lithospheric mantle), and Al-poorer rims without Fe^{3+} (related to the final stage of exhumation). In contrast, garnets have $Fe^{3+}/\Sigma Fe$-poor cores (<0.03) and slightly higher ratios in the rims (0.04–0.07). When considered together with the markedly higher Fe^{3+} contents in the earliest clinopyroxene generation, this pattern is consistent with a pressure–temperature–dependent partitioning of ferric iron from garnet to clinopyroxene during cooling from 1100 to 950 °C along the exhumation path. fO_2 calculations suggest a variation from more oxidised samples (ΔFMQ = −1.25 to 0) to more reduced ones (ΔFMQ = −4.2 to −1.6) at 3 GPa. At 1.5 GPa, ΔFMQ ranges from −1.2 to −0.6 down to < −5, indicating that graphite may have formed through reduction of a previously oxidised carbon phase. The oxidation state variations are linked to sub-solidus

* Corresponding author.
E-mail addresses: nadia.malaspina@unimib.it (N. Malaspina), falko.langenhorst@uni-jena.de (F. Langenhorst), kilian.pollok@uni-jena.de (K. Pollok), valerio.cerantola@unimib.it (V. Cerantola), mara.murri@unipv.it (M. Murri), c.longa1@campus.unimib.it (C. Longa), danilo.bersani@unipr.it (D. Bersani), alessandra.montanini@unipr.it (A. Montanini).

https://doi.org/10.1016/j.chemgeo.2025.123173
Received 22 October 2025; Received in revised form 28 November 2025; Accepted 30 November 2025
Available online 1 December 2025

decompression, and not to S-C-related redox reactions, describing a closed system with no fluid/melt-rock interaction. Our results show that sulphur plays no role in controlling the redox state of these graphite-bearing mantle rocks, even over prolonged geological histories, and that variations in the redox state of carbon and iron in garnet and clinopyroxene can depend on pressure and temperature changes only, rather than from redox reactions, indicating that the intensive variable fO_2 can be decoupled from redox processes in a closed system.

1. Introduction

The history of Earth's atmosphere has been defined by variations in O_2 levels, which strongly affected the evolution and development of life on the Earth (Berner, 2003). Changes of O_2 and CO_2 concentrations can be closely related to the composition of volatiles released to the atmosphere from magmatic activity that may occur at ocean ridges, during intraplate magmatism (e.g. Large Igenous Provinces) or in correspondence of subduction zones. Andrault et al. (2017) also proposed that the development of stable, deep subduction systems after the Archean–Proterozoic transition may have favoured the release of an excess of oxygen to the Earth's surface, initially trapped in the deep mantle in the form of primordial Fe^{3+} excess. The oxygen concentration in the atmosphere also depends on the long-term carbon cycle, as for example the high O_2 levels and low CO_2 levels during the Permo-Carboniferous, shown by Berner (2003). Most of Earth's carbon is hidden in the mantle. Indeed, the recycling of carbon into the convecting mantle has proven to be an efficient process, accounting for a significant fraction of the total carbon outgassed at ridge and intraplate boundaries (Hirschmann, 2018), but we do not know the extent of the main deep reservoirs and the mechanism by which carbon moves from one repository to another. Also, the stability of graphite/diamond, relative to the more reactive CO_2 or carbonates is controlled by the oxidation state of the mineral assemblages and by the role of sulphur in its different oxidation states (e.g., Gunn and Luth, 2006; Palyanov et al., 2007; Evans, 2006, 2012; Bénard et al., 2018). For this reason, in the last decades many efforts have been devoted to the understanding of the redox state of the convective mantle, and in particular of mantle peridotites, both xenoliths and orogenic peridotites (e.g., Wood et al., 1990; Canil et al., 1994; Brandon and Draper, 1996; Canil and O'Neill, 1996; Simakov, 1998; Woodland et al., 2006; Malaspina et al., 2009, 2010, 2012; Foley, 2011; Yaxley et al., 2012; Hanger et al., 2015; Rielli et al., 2017). However, the upper mantle also includes layers of pyroxenites that may have an important role in the element exchange and in the rheological behaviour of mantle peridotites hosting them, particularly at the slab-mantle interface (Berly et al., 2006; Wang et al., 2008; Malaspina et al., 2017, 2023; Pellegrino et al., 2020, 2021), in the dynamic mantle wedge (Notini et al., 2024), and in the deep cratonic mantle (e.g., Kopylova et al., 1999; Aulbach and Smart, 2023; Aulbach and Jacob, 2016; Aulbach et al., 2020, 2024).

Many of the pyroxenites from sub-cratonic mantle xenoliths and those from off-craton orogenic mantle peridotites have been interpreted as derived from the recycling of deep and ancient crustal materials. One of the most extensively studied terranes include the ultramafic orogenic massifs of Ronda (Spain) and Beni Bousera (Morocco), which belong to the Betic-Rifian fold belt, now separated by the Alboran Basin (Davies et al., 1993). In both ultramafic massifs layers of pyroxenites were interpreted as derived from the crystallisation of melts from deep origin, in turn derived from subducted eclogitic gabbros (e.g., Kornprobst et al., 1990; Pearson et al., 1993; Pearson and Nowell, 2004; Marchesi et al., 2013). A similar interpretation has been also proposed for the External Ligurian pyroxenites from the northern Appennines (Italy), which occur in the subcontinental lithospheric mantle exhumed during the opening of the Jurassic Ligurian-Piedmontese basin (Montanini et al., 2006, 2012; Montanini and Tribuzio, 2015). Similar to Ronda and Beni Bousera pyroxenites, garnet clinopyroxenites from this location contain graphite and sulphides in equilibrium with garnet and clinopyroxene (Montanini et al., 2010) and formed from the crystallisation of eclogite-derived melts (Montanini et al., 2012). The precursors of these melts were Mid Ocean Ridge (MOR-type) gabbroic protoliths which experienced a long-lived evolution of recycling into the mantle (~1.0–1.5 Ga ago, Montanini and Tribuzio, 2015). These graphite-sulphide-bearing pyroxenites therefore represent one of the three unique case studies worldwide as a proxy of deep carbon and sulphur recycling from crustal materials in relation to the redox evolution of the crust in the Archean-Proterozoic boundary, when subduction started to become the dominant mechanism for mantle mixing and oxygen increase toward the modern atmosphere (e.g., Andrault et al., 2017).

In this work we show the redox evolution of carbon- and sulphur-bearing orogenic garnet clinopyroxenites from off-craton mantle, retrieved from cutting-edge high-resolution in-situ Fe^{3+} measurements in both garnet and clinopyroxene. We identify different generations of clinopyroxene, each equilibrated with sulphides, and likely two generations of carbon phases. The earliest clinopyroxene generation was probably in equilibrium with a carbonate phase, whereas the latest appears to have equilibrated with graphite. We discuss (i) the role of Fe^{3+} garnet/clinopyroxene partitioning in orogenic mantle pyroxenites (usually investigated in mantle peridotites) that recorded a long-lived and complex history as proxy of heterogeneities in the convective mantle, (ii) the contribution of a detailed petrologic study in retrieving the redox evolution of deeply recycled crustal material and (iii) its role in the carbon and sulphur cycles.

2. Geological background and sample description

The garnet clinopyroxenites studied in this work belong to the External Ligurian ophiolites from the Alpine-Apennine belt, a lithospheric remnant of the Jurassic Western Tethys (Ligurian-Piedmontese basin). Here, the pyroxenites occur as layers within fertile mantle peridotite bodies (Rampone et al., 1995; Müntener et al., 2004). The External Ligurian ophiolites were considered to have derived from the lithosphere of the Ligurian-Piedmontese basin and its transition to the Adria continental margin (Marroni et al., 2002). Differently, other Alpine-Apennine ophiolites (Internal Ligurides, Lower Platta, S Tuscany and Monte Maggiore) formed after the opening of the Ligurian Tethys in the Middle Jurassic and display structural and compositional similarities to the oceanic lithosphere from slow and ultra-slow spreading ridges (Tribuzio et al., 2004; Rampone et al., 2008; Piccardo, 2008; Manatschal and Müntener, 2009).

The External Ligurian (EL) ophiolites consist of meter to kilometre-sized bodies of fertile spinel-plagioclase lherzolites, prevailing MOR-type basalts and rare gabbroic rocks embedded in sedimentary mélanges of Upper Cretaceous age (Marroni et al., 2017). The EL mantle section has been further subdivided into three mantle domains, developed during the Mesozoic rifting evolution (Ferrari et al., 2022): (i) an undeformed spinel tectonite domain, characterised by static plagioclase crystallisation; (ii) a plagioclase mylonite domain recording melt-absent deformation, and (iii) a nearly undeformed plagioclase-rich melt-impregnated domain. The samples studied in this work belong to the mylonite domain (i), which consists of partially serpentinised peridotites characterised by a mylonitic fabric and large pyroxene porphyroclasts. These peridotites host different pyroxenites layers: most frequent thin websterites (2–10 cm thick) and rare garnet clinopyroxenites (up to 2 m thick) that are concordant with the mylonitic foliation, sharing sharp

contacts with the peridotites (Montanini et al., 2006). While the websterites are generally boudinaged and stretched, the garnet clinopyroxenites, in the centre of the thickest layers, are mostly isotropic, coarse-grained and only show a weak foliation in the external portions of the layers. The garnet clinopyroxenites record an early stage of equilibration in the subcontinental lithosphere at P = 2.8–3.0 GPa and T = 1100–1150 °C (Montanini et al., 2006). One sample of garnet clinopyroxenite also provided Lu—Hf and Sm—Nd mineral isochrons of 220 ± 13 Ma and 186 ± 1.8 Ma, respectively, interpreted to reflect a slow cooling evolution in response to the rifting process that led to the opening of the Western Tethys (Montanini et al., 2006).

The studied samples (BA-X, BA-Xs, BA2-XX, BA-2A, BAR-A, AM321B, AM384) were collected from adjacent portions of the inner part of a metre-thick garnet clinopyroxenite layer from Rio Strega locality (see Fig. 1 of Montanini et al., 2006). The samples mainly consist of pinkish Al-rich clinopyroxene (augite) commonly displaying plagioclase exsolution lamellae. In the garnet stability field, the clinopyroxene was characterised by high Al_2O_3 and Na_2O contents (Montanini et al., 2006) and exsolutions of clinoenstatite lamellae (see section 4.1). Clinopyroxenes are slightly oriented and surround red-orange garnets, which locally include un-exsolved Al-rich clinopyroxene and are surrounded by greenish pyroxene + spinel kelyphitic coronas (Fig. 1a). High temperature graphite in textural equilibrium with clinopyroxenes (Fig. 1b) occurs as euhedral flakes and stack of flakes (up to 2–3 mm). The mineral assemblage also includes accessory Fe–Ni–Cu sulphides occurring both as inclusions in silicates and graphite, and as interstitial grains (Fig. 1c). Sulphides included in garnets are frequently surrounded by haloes of tiny multiphase fluid inclusions (Fig. 1d), likely related to a decrepitation of a partially molten sulphide (Montanini et al., 2010). These samples also locally contain garnet-free granoblastic domains characterised by orthopyroxene, Al-poor clinopyroxene, plagioclase and spinel (Montanini et al., 2006). All the samples analysed in this work are from "type-A" garnet pyroxenites (Montanini et al., 2012), characterised by LREE depletion and nearly flat HREE, showing a small positive Eu anomaly.

In summary, the analysed clinopyroxenites display three generations of clinopyroxenes: (i) high pressure (>3 GPa) un-exsolved crystals included in garnet cores (Fig. 1a and Table S1), (ii) clinoenstatite exsolution-bearing grains related to a first stage of exhumation in the lithospheric mantle (Fig. 1a and 2) and (iii) Al-poorer rims in equilibrium with garnet rims related to the final stage of exhumation (1.5 GPa; Table S1).

Geochemical and isotopic studies on these garnet clinopyroxenites demonstrated that their origin was related to crustal recycling, involving melting of gabbro-derived eclogites (Montanini et al., 2012). Montanini and Tribuzio (2015) subsequently proposed the pyroxenite petrogenesis occurred through i) recycling of a MOR-type heterogeneous gabbroic sequence into the mantle 1.5–1.0 Ga ago; ii) melting of the eclogitised gabbros; (iii) crystallisation in the astenospheric mantle and subsolidus re-equilibration triggered by Mesozoic rifting. It is worth of note that where no interaction with the host peridotites occurred, the crystallisation of such melts formed garnet clinopyroxenites, whereas the websterites record melt-peridotite hybridization processes. Notably, the host peridotites and the other pyroxenite types in the same mantle section do not contain any C-bearing mineral phases (Montanini et al., 2010).

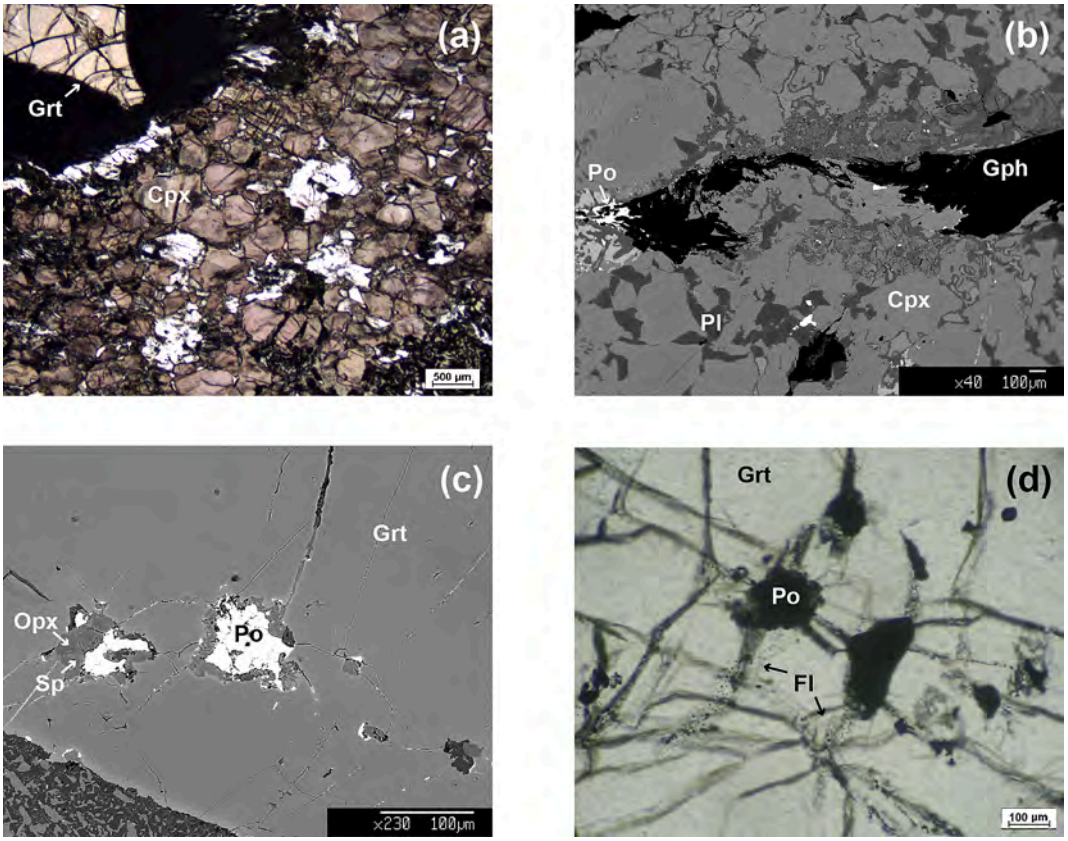

Fig. 1. Optical micrograph (a-d) and back-scattered electron (BSE) images (b-c) of EL clinopyroxenites. (a) Plane polarized light (PPL) photograph of pink Al-rich clinopyroxenes surrounding coarse garnet, locally rimmed by orthopyroxene+ spinel + plagioclase retrograde kelyphite. (b) BSE image of elongated graphite parallel to the pyroxenite weak foliation, associated with iron sulphides, clinopyroxene and rare quartz. (c) BSE image of sulphides inclusions in garnet along with orthopyroxene + spinel symplectites in the inclusion interface. (d) PPL image showing fluid inclusions decrepitation haloes and trails around sulphides inclusions. Abbreviations: Gph = graphite; Cpx = clinopyroxene; Pl = plagioclase; Grt = garnet; Opx = orthopyroxene; Sp = spinel; Po = pyrrhotite; FI = fluid inclusion. (For interpretation of the references to colour in this figure legend, the reader is referred to the web version of this article.)

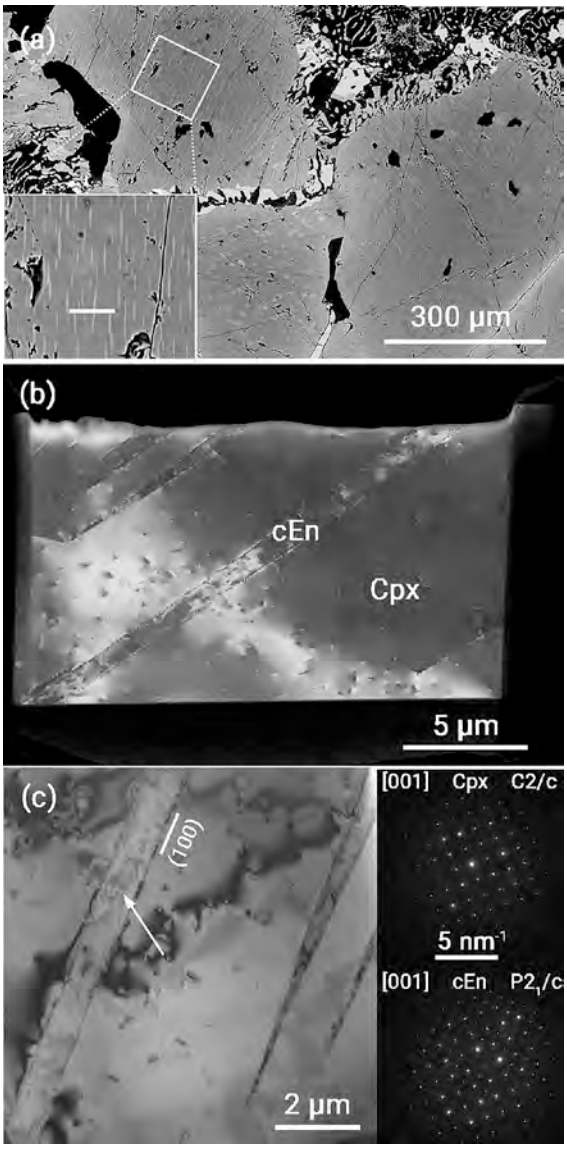

Fig. 2. (a) BSE image of clinoenstatite (cEn) exsolutions in Al-rich clinopyroxene (Cpx) matrix. The enlarged inset shows the position of the FIB preparation which was initially 30 µm long. (b) LM-STEM dark-field image (diffraction contrast) of the entire FIB cut showing cEn exsolution lamellae with interfaces decorated by dislocations from structural misfit and free dislocations in the clinopyroxene matrix. (c) Bright field TEM image and diffraction patterns of matrix and exsolution. The lamellae are parallel to the (100) plane of both phases. The arrow marks areas with visible antiphase domains from the C2/c to $P2_1/c$ transition of clinoenstatite.

3. Analytical methods

3.1. Electron microprobe analyses

Major element compositions of garnets, clinopyroxenes and retrograde phases, along with inclusions in garnets, were analysed by wavelength dispersive spectrometry using a Jeol 8200 Super Probe at the Department of Earth Sciences, University of Milano. Acceleration voltage was set to 15 kV, beam sample current was 5 nA and 1 µm beam diameter. Natural standards used were omphacite (Na), grossular (Ca, Al, and Si), fayalite (Fe), olivine (Mg), orthoclase (K), rhodonite (Mn), ilmenite (Ti), niccolite (Ni) and pure Cr (Cr). A counting time of 30 s was used for all elements. A PhiRhoZ routine was used for matrix correction. Representative results and the corresponding microstructural positions, corrected for the measured Fe^{3+} (see below) are reported in Table S1.

3.2. Analytical transmission electron microscopy and electron energy loss spectroscopy

Transmission Electron Microscopy (TEM) investigations were performed at the Friedrich Schiller University Jena. Double polished thin sections of clinopyroxenite samples were used for the preparation of TEM foils. 3 mm wide Cu grid were glued onto areas of interest and then thinned to perforation by Ar ion milling in a Gatan Duomill ion milling machine at 4.5 kV and 1 mA and an incidence angle of 13°, until electron transparency was reached.

Specific areas of interest in clinopyroxene and garnet were identified by back-scattered electron (BSE) images and prepared for TEM using a FEI Quanta 3D FEG focused ion beam (FIB-)SEM instrument at Friedrich Schiller University Jena (Fig. 2). The Ga ion gun was operated at 30 kV with a beam current between 30 and 0.1 nA for sample preparation. A deposited Pt stripe was used to protect the surface. To remove amorphous layers on the FIB cut, the foils were cleaned at 5 kV using 48 pA beam current.

TEM foils were imaged by conventional techniques (bright-field and dark-field) and high-resolution techniques, in combination with selected area electron diffraction (SAED), using a 200 kV FEI Tecnai G2 F20 TEM. To collect complete images of the FIB sections for lattice defects and exsolutions, we have also used the high-angle annular dark-field (HAADF) detector at low magnification scanning transmission electron microscopy (LM-STEM) mode with a very long camera length to obtain diffraction contrast images. Energy-dispersive X-ray (EDX) emission spectra were acquired to obtain the compositions of the minerals and their exsolutions using an Oxford X-MaxN 80 T SDD system. These analyses were quantified based on the principle of electroneutrality by considering an absorption correction (van Cappellen and Doukhan, 1994; Langenhorst et al., 1995) and the $Fe^{3+}/\Sigma Fe$ ratios measured by Electron Energy Loss Spectroscopy (EELS). EELS was employed to analyse clinopyroxene (both included in garnet and in the rock matrix, along with clinoenstatite exsolutions) and garnet profiles (Fig. 3), using a Gatan Quantum GIF mounted to the TEM. The quantification of $Fe^{3+}/\Sigma Fe$ ratios was based on the white line intensities of the Fe L_{23} edges, which are well calibrated for garnets and oxidic minerals (van Aken et al., 1998; van Aken and Liebscher, 2002). Fe L_{23} ELNES spectra were measured with an energy dispersion of 0.1 eV per channel in the diffraction mode of the TEM and corrected for dark current and channel-to-channel gain variation of the detector. The energy resolution, measured as width of the zero-loss peak at half maximum, was 0.8–0.9 eV. To extract the pure single-scattering core-loss signal, an inverse power-law background was subtracted, and multiple-scattering contributions were removed by the Fourier-ratio technique. Errors in the $Fe^{3+}/\Sigma Fe$ ratio are usually estimated to be on the order of 0.03–0.04, if the iron concentration is greater than 5 wt% (van Aken et al., 1998; van Aken and Liebscher, 2002; Frost and Langenhorst, 2002; Malaspina et al., 2010, 2012). For iron concentrations around 3 wt%, the uncertainty, expressed as 1σ, has been estimated to be 0.08 (Frost and Langenhorst, 2002).

3.3. Synchrotron Mössbauer spectroscopy

In situ Synchrotron Mössbauer Spectroscopy (SMS) data (^{57}Fe spectra) were collected on double polished thin sections (≈ 150 µm; Table S1) at the Nuclear Resonance beamline (ID18) at the European Synchrotron Radiation Facility (ESRF, Grenoble, France) where the SMS is based on a monochromator that uses pure nuclear reflections from an iron borate ($^{57}FeBO_3$) crystal to achieve nuclear resonant resonance. The source produces the required ^{57}Fe resonant radiation at 14.4 keV and within a bandwidth of 15 neV, which is tuneable over a range of approximately 0.6 eV. The SMS's beam of radiation has a high brilliance, is almost entirely resonant and totally polarized and can be focused to a

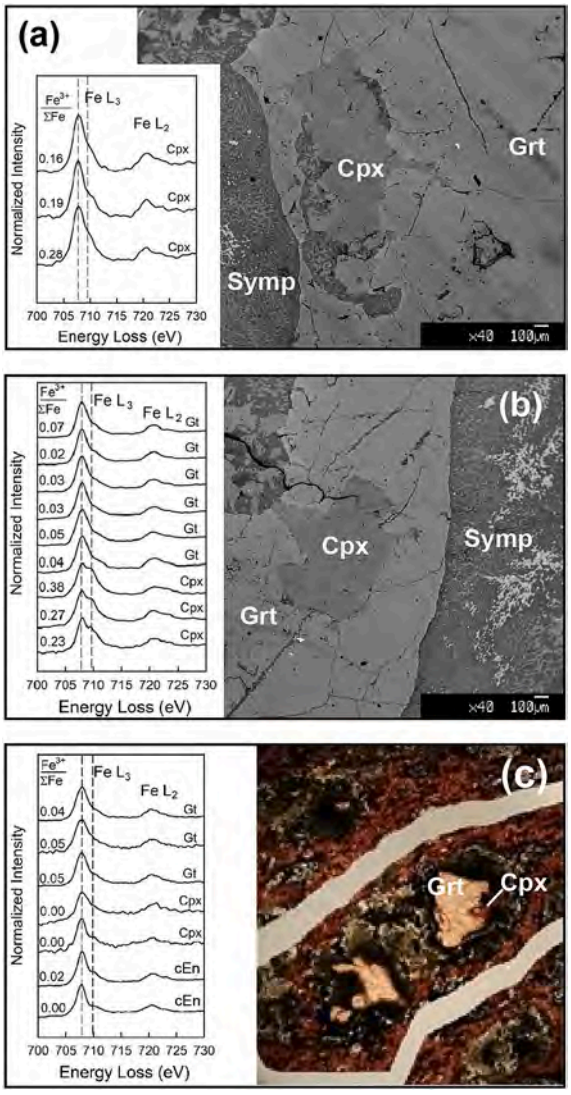

Fig. 3. Representative spectra of Fe L_{32} electron energy-loss near-edge structure (ELNES) of garnet and clinopyroxenes of samples BA2-XX (a, b), and BA-X (c). The spectra have been normalised to their maximum intensity and shifted vertically for comparison. Dashed lines mark the energy positions for the Fe L_3 peaks representative for the Fe^{2+} (707.8 eV) and Fe^{3+} (709.5 eV) content. BSE images of BA2-X and thin section photograph of BA-X reports the measurements sites. Symp = symplectite.

spot size of 10 µm by 5 µm. The Confocal Beryllium lenses (CRLs) are used to prefocus the X-ray beam to a lower beam width. Moreover, a Beryllium window is placed along the beam path, which is used to maintain the vacuum in one of the monochromator chambers and while allowing the X-rays to pass through with the least amount of attenuation (Potapkin et al., 2012). Both Be-window and CRLs must be considered since iron is an element that is always present in trace amounts beryllium metal, despite having an extremely low intensity due to the extremely low iron contamination content, and this can be done by adding a known and constant additional element during the fitting process. Indeed, the hyperfine parameters that define the Be-components can be manually entered in the fitting program, Syncmoss (Yaroslavtsev, 2023). The hyperfine parameters of the clinopyroxenes and garnets of the selected samples are reported in Table S2. The Be-components of the lenses are: 0.091 (center shift), −0.52 (quadrupole splitting) and 0.787 (asymmetry).

The collection time for one spectrum was approximately of two hours, which is extremely fast considering that the samples were not enriched in ^{57}Fe atoms. The velocity scale of all Mössbauer spectra was set at 5 mm/s and was calibrated relative to 25 µm-thick α-Fe foil. All spectra were fitted using the software package Syncmoss (Yaroslavtsev, 2023). Lorentzian lines were used to fit all Mössbauer spectra, and a linear function was applied to model the background. All spectra were fit using the full transmission integral to avoid distortion of the area ratios and representative fittings are reported in Table S2 and Fig. 4. The estimated errors based on multiple iterations of spectra fitting are within ±0.01 for Grt and ± 0.03 for Cpx (see Table S2).

3.4. Raman spectroscopy

Non-polarized Micro-Raman spectra were collected on some thin sections (both double polished and mounted on glass) obtained from the samples in a nearly backscattering geometry with a Confocal Horiba LabRAM HR Evolution confocal spectrometer (focal length 800 mm), using a configuration with a 600 lines mm^{-1} grating, a set of Bragg ultra-low frequency filters for the rejection of the Rayleigh scattering for the 632.8 nm excitation or a dielectric edge filter for the excitation at 532 nm, and a liquid nitrogen-cooled CCD detector. An optical 100× objective was used to obtain a spatial resolution of ≈ 1 µm, with ≈ 1 cm^{-1} resolution. Typical collection time for the confocal configuration was 30 s for each acquisition, with 2–4 repetitions. The power on the sample was kept under 10 mW using neutral density filters. Before each measurement session, the spectral position was calibrated using the main Raman band of silicon. On few selected regions, Raman micro-mappings have been obtained using the motorized XY stage of the instrument (Fig. 5). The fitting of the Raman spectra was performed after the background subtraction using a Gauss-Lorentzian function in the LabSpec 5 © software. This allowed the determination of Raman spectrum parameters as peak position, full-width-at-half-maximum and the area of the peak.

3.5. Thermodynamic modelling

We calculated log fO_2–T sections at different pressures in the MgO + FeO + CaO + Al_2O_3 + Na_2O + SiO_2 + S_2 + C system, for a fixed bulk composition measured by X-ray Fluorescence (MgO = 12.11 wt%, FeO = 10.46 wt%, CaO = 12.07, Al_2O_3 = 18.74, Na_2O = 1.36, SiO_2 = 44.60 wt%, S_2 = 0.80 wt%, C = 2.00 wt%) of a representative sample from group "BA", employing the Perple_X software package (version 7.1.5; Connolly, 2005). We used the internally consistent thermodynamic database of Holland and Powell (2011) revised in 2017 and the following solid solution models: ternary feldspars (Pl, Holland and Powell, 2003), olivine and spinel (O, Sp, Holland and Powell, 1998), orthopyroxene (Opx, Powell and Holland, 1999), garnet (Gt, Holland et al., 2018), clinopyroxene (Cpx, Green et al., 2016), pyrrothite (Po, Holland and Powell, 2011) and carbonates (Do, Franzolin et al., 2011). No phase has been excluded.

4. Results

4.1. Mineral chemistry of clinopyroxenes and garnets, and micro-Raman of mineral inclusions

The major element compositions of the analysed clinopyroxenes and garnets of the selected samples, along with $Fe^{3+}/\Sigma Fe$ and calculated logfO_2, are reported in Table S1. Representative profiles and variation diagrams are reported in Tables S3 and S4, and in Fig. 6.

Clinopyroxenes mostly correspond to diopside and augite. Clinopyroxenes included in garnet that do not show exsolution lamellae have a homogeneous composition (Table S3), whereas exsolved clinopyroxenes, both included in garnets and in the rock matrix, show a patchy zonation (Fig. 6a, c) characterised by a core-to-rim increase in Ca, and by the complementary decrease in Al and Na (all in atoms per formula units, a.p.f.u.). The inhomogeneous zonation, characterised by local

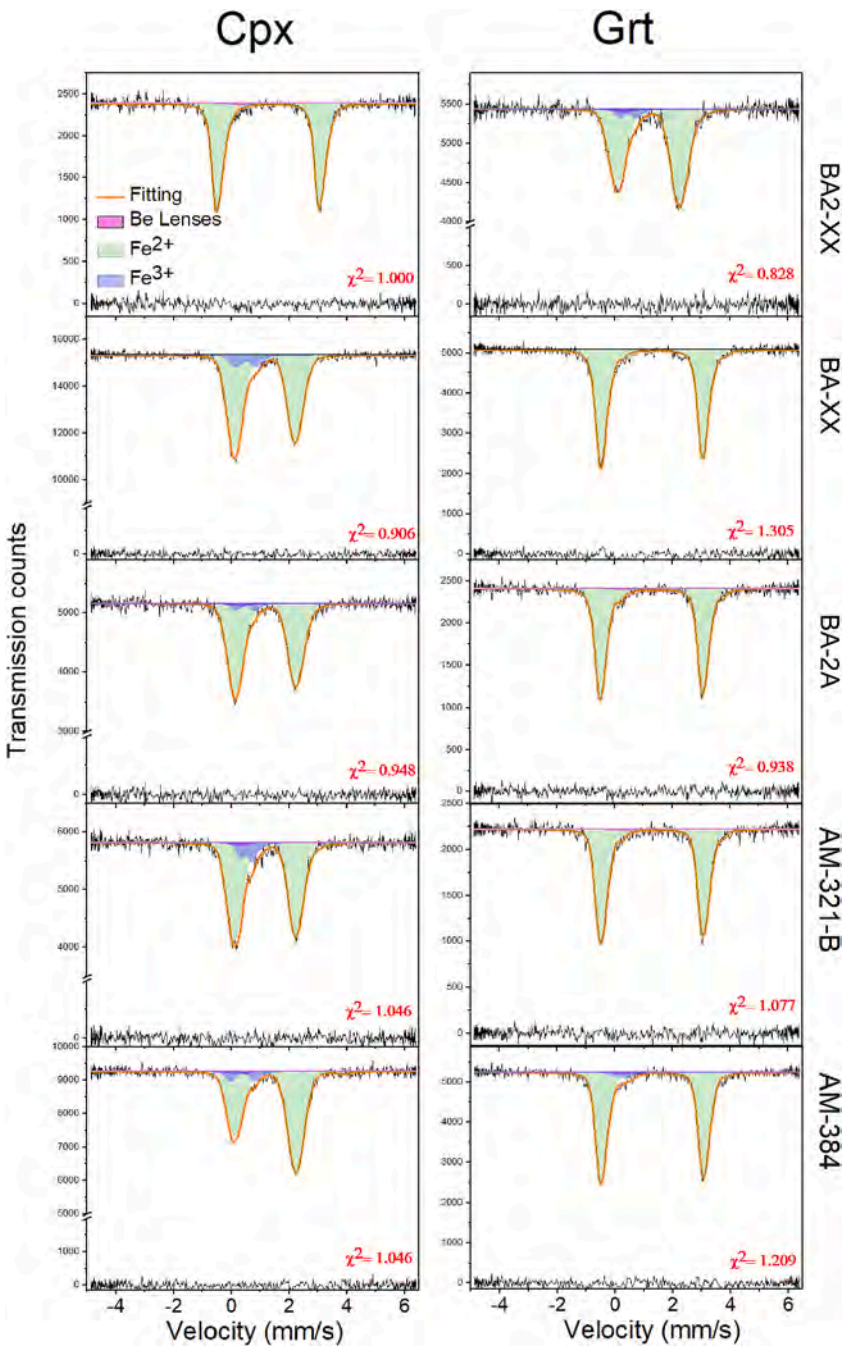

Fig. 4. Representative SMS spectra of clinopyroxenes and garnets from samples BA-2XX, BA-XX, BA-2 A, AM-321-B and AM-384. The black line is the raw spectrum; the resulting fitting is the orange line. Be lenses contribution is displayed in pink, while the Fe^{3+} and Fe^{2+} doublets are in blue and green, respectively. (For interpretation of the references to colour in this figure legend, the reader is referred to the web version of this article.)

decrease in Ca, Al and Na, and a complementary increase in Fe and Mg may be related to the occurrence of clinoenstatite exsolutions (Fig. 2b) and/or to a sub-grain recrystallisation. As shown in Fig. 6e, clinopyroxenes included and those at the contact with garnet show the highest content in Na with jadeite (Jd) component higher than clinopyroxenes in the rock matrix (22 mol% vs 3–13 mol%). The variation of Jd composition is not correlated with Ca-Tschermak (Ca-Ts; Table S1), but there is a correlation between total Al and 2Na (a.p.f.u.), where clinopyroxenes in sample AM384 and those included in graphite porphyroblasts reach the lowest Al—Na concentrations, indicating that they crystallised at lower P-T conditions, during the cooling and exhumation.

The garnet compositions, considering the total iron as Fe^{2+}, show variable almandine (Alm = 30–36 mol%), grossular (Grs =18–20 mol%) and pyrope (Prp = 48–51 mol%) contents. Garnet measured with EELS and SMS show slightly variable concentrations of andradite (Andr) between 0 and 1 mol% (Table S1). The Prp, Alm, Grs and spessartine (Sps) concentrations in garnet do not show any important core-to-rim variation, except for a very thin rim at the contact with included clinopyroxene and the outermost rim (Fig. 6b, d). This zonation shows an increase in Alm and a decrease in Prp which are likely related to retrograde equilibration and to a partitioning with clinopyroxene. All the samples, although collected in the same meter-thick vein, show a linear correlation between Grs and Alm, likely indicating a re-equilibration at lower P-T conditions, similarly to clinopyroxenes (Fig. 6f).

Multiphase fluid inclusions have been analysed by micro-Raman

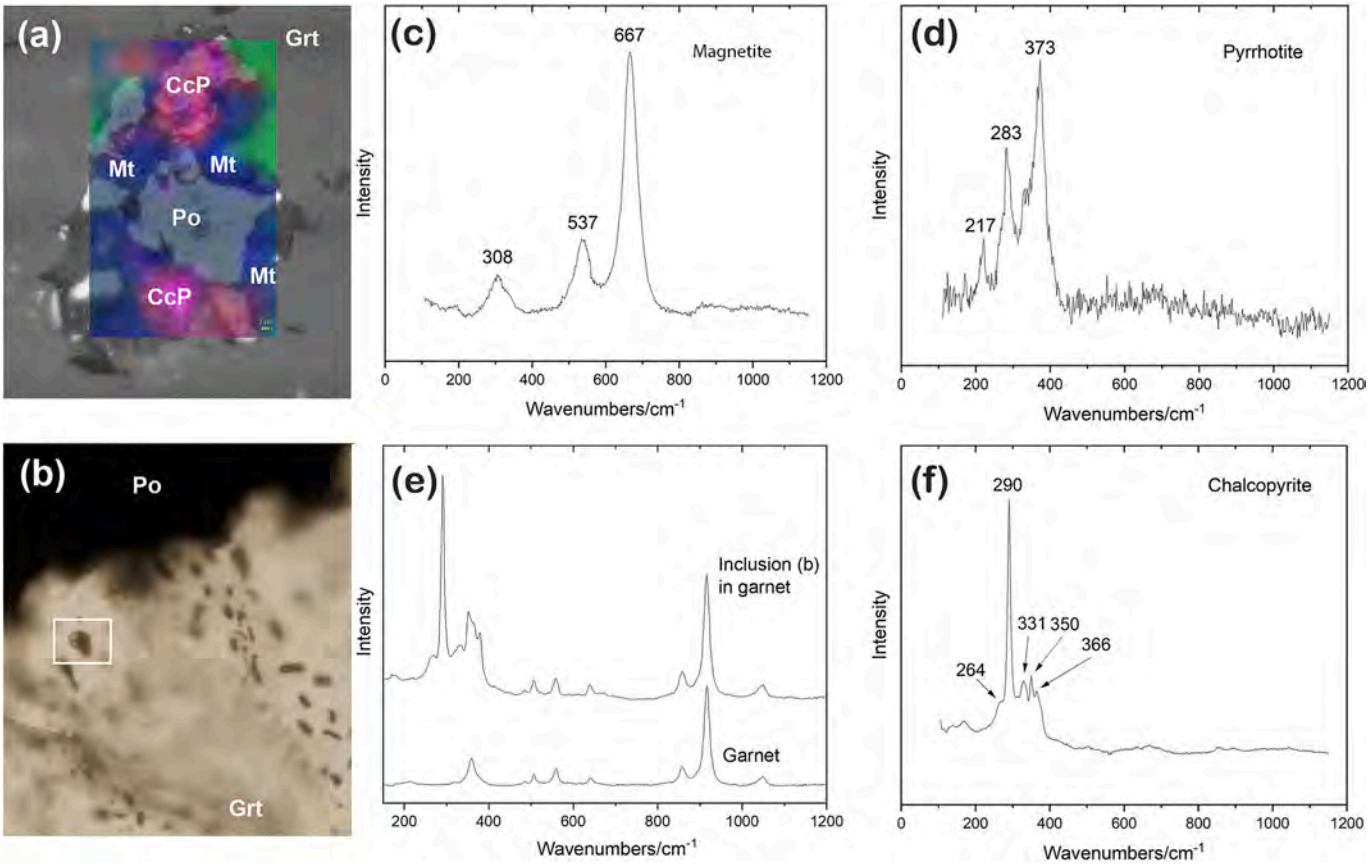

Fig. 5. Optical microscope image and false-colours Raman mapping of a polyphasic inclusion (a) and optical microscope image of some minor inclusions (b). Representative Raman spectra of the main minerals found in the inclusions: (c) magnetite, (d) pyrrhotite, (e) spectrum of the inclusion (white square ~ 20 × 30 μm) in Fig. 5b) "as obtained", including the spectrum of the host garnet (also reported), (f) spectrum of the chalcopyrite present in the inclusion (b) after the subtraction of the garnet spectrum. Abbreviations: CcP = chalcopyrite; Mt. = magnetite; Po = pyrrhotite; Grt = garnet.

(Fig. 5). We measured different kinds of inclusions, small ones, with few micrometres of diameter, and larger ones, with metallic aspect. In every case, the Raman spectra were dominated by the signal of the host garnet, typical of a pyralspite with pyrope as the main endmember (main peaks at 916, 360, 858, 559 cm^{-1}), as determined using the "Miragem" software (Bersani et al., 2009). The main peaks of pyroxenes were sometimes present too. After a proper subtraction of the garnet spectral features, the minor inclusions usually show the Raman features of chalcopyrite (Fig. 5f). Larger inclusions usually are composed of different phases including magnetite (Fig. 5c), pyrrhotite (Fig. 5d) and chalcopyrite (Fig. 5f). A Raman micro-map was acquired in one of those large inclusions and the results are shown in false colours in Fig. 5a.

4.2. $Fe^{3+}/\Sigma Fe$ of clinopyroxenes and garnets

The analysed garnet clinopyroxenites show at least three generations of clinopyroxenes: (i) un-exsolved crystals included in the garnet cores, with homogeneous and higher Jd concentration, (ii) clinoenstatite exsolution-bearing grains (both included in garnet and occurring in the rock matrix) and (iii) Al-poorer rims along with tiny crystals included in graphite (Fig. 6e). As shown in Table S1, EELS and SMS measurements show that clinopyroxenes included in garnets have relatively high $Fe^{3+}/\Sigma Fe$ ratios (0.16–0.38), the matrix crystals show a zonation with higher $Fe^{3+}/\Sigma Fe$ in the cores (0.03–0.10) and no detectable Fe^{3+} in the rims (Fig. 3c and 4), and the clinoenstatite exsolution has $Fe^{3+}/\Sigma Fe$ ranging between below detection limit and 0.02 (Fig. 3c). Fig. 7a displays a poorly defined and scattered relationship between $Fe^{3+}/\Sigma Fe$ and the Jd component in clinopyroxenes. Two rim analyses deviate from this trend, showing relatively high Jd mol.% but $Fe^{3+}/\Sigma Fe$ below detection limits. This can be the result of a bias in the recalculation, considering that Na may be incorporated both as Aeg and Jd components (Woodland, 2009; Malaspina et al., 2012). Indeed, the increase of Jd content does not follow the 1:1 dashed correlation line. Figs. 7a, b and d also include data for samples of pyroxenites, gabbro-derived eclogites and variable Mg-Ca-bearing eclogites from Zimbabwe and Siberia sub-cratonic xenoliths reported by Aulbach et al. (2020, 2022). Although cratonic xenoliths represent a different tectonic setting, they also originated as deeply subducted oceanic crust (Aulbach and Smart, 2023) and illustrate the behaviour of garnets and clinopyroxenes at great depths, allowing a comparison to our Fe^{3+} measurements of garnets and clinopyroxenes from off-craton mantle pyroxenites. Note that pyroxenites from Orapa (green squares) fall in a good trend with our samples (Fig. 7a). The relationship between calculated ΔFMQ (see section 5.1) and Al^{IV} in our clinopyroxenes is weak within our dataset because Al^{IV} remains nearly constant in most samples, except for AM-384 and two analyses from BA-X (Fig. 7b). However, when compared with clinopyroxenes from Orapa and Udachnaya, the relative evolution of ΔFMQ with decreasing temperature is similar. The apparent flattening of the trend in our samples reflects their much higher Al^{IV} values (0.13–0.26) compared to cratonic xenoliths (0.00–0.05), which shifts the correlation to a different compositional range.

Differently from clinopyroxenes, garnets show $Fe^{3+}/\Sigma Fe$ poor cores (bdl-0.03) and higher ratios in mantle and rims (0.04–0.07). The negative correlation between Fe^{3+} and Al (a.p.f.u.), related to their substitution in the garnet octahedral site is evidenced in Fig. 7c and fall along the same correlation with other samples of subduction-derived metasomatic orthopyroxenites and websterites from Maowu ultramafic complex (China) and Bardane in the Norwegian Western Gneiss Region.

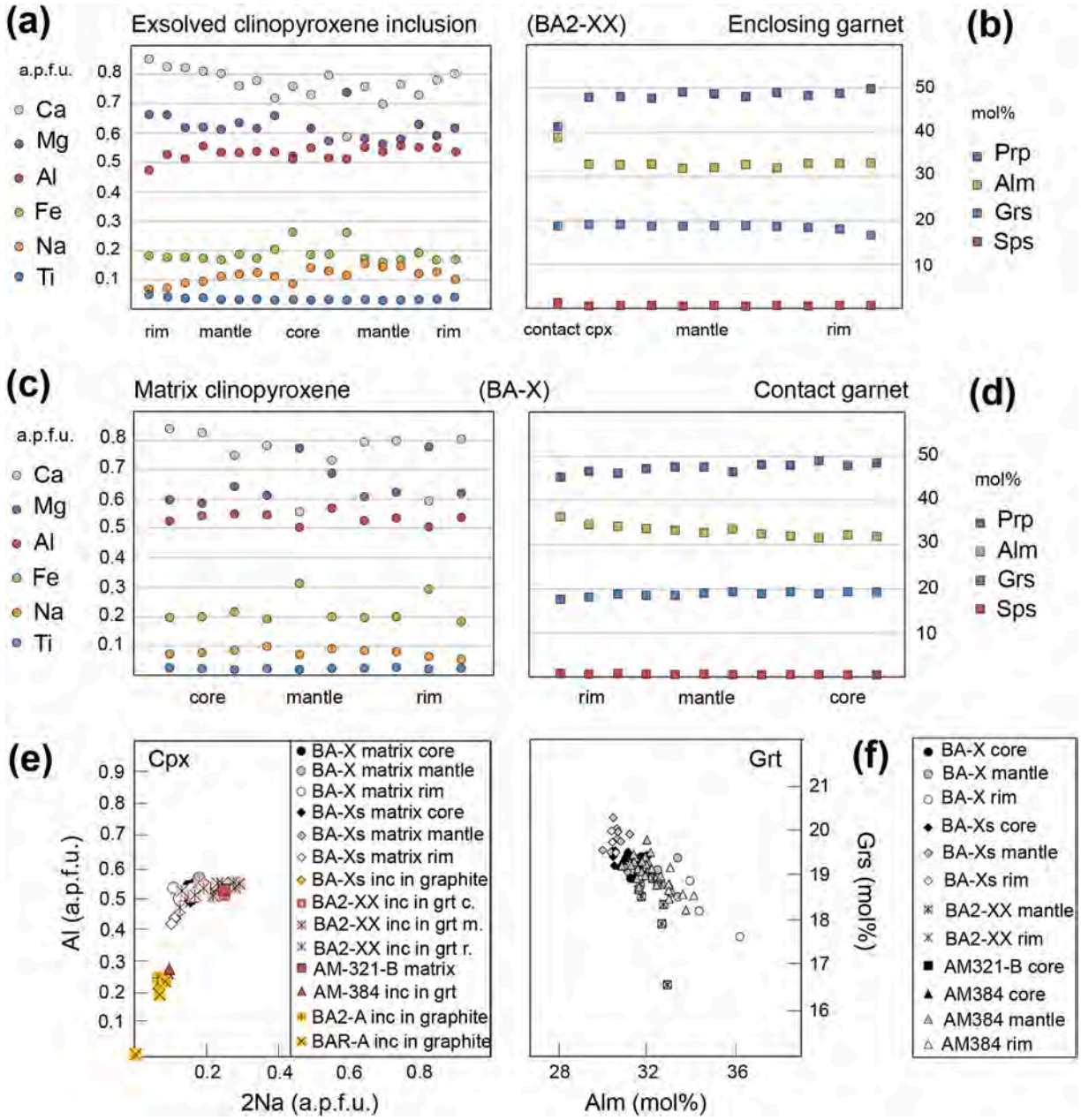

Fig. 6. (a, b, c, d) Compositional profiles of representative clinopyroxenes and garnets: (a) exsolved clinopyroxene included in porphyroblastic garnet (b), where the right boarder of clinopyroxene is in contact with the left boarder of the enclosing garnet; (c) exsolved coarse clinopyroxene in the rock matrix, in contact with porphyroblastic garnet (d). The line analyses and micrographs of the relative positions are reported in Table S2. (e) Variation diagram (total Al vs 2Na in atoms per formula units) of all the analysed samples and relative microstructural positions. Inc. = inclusion; c. = core; m. = mantle; r. = rim. (f) Variation diagram (grossular vs almandine mole percentage, calculated considering total iron as Fe^{2+}) of all the analysed samples. The complete datasets are reported in Tables S3 and S4.

As said before, the complementary core-to-rim decrease and increase of $Fe^{3+}/\Sigma Fe$ in clinopyroxenes and garnets, respectively, of EL samples may be related to a decrease of P and T during the exhumation from (at least) 3 GPa and 1100 °C to 1.5 GPa and 950 °C, leading to the formation of spinel + plagioclase symplectites between garnet and clinopyroxene (Montanini et al., 2006). This partitioning related to different equilibration conditions is well shown in Fig. 7d, that displays the $Fe^{3+}/\Sigma Fe$ in clinopyroxene and garnet couples at microstructural equilibrium and the relative andradite and aegirine components in the inset. The samples from cratonic xenoliths also show a strong partitioning of Fe^{3+} into clinopyroxene with respect to garnet, indicating that the use of Fe^{3+} content only in garnet to retrieve the fO_2 could be strongly biased. Indeed, Woodland (2009) modelled the garnet–clinopyroxene equilibrium in garnet peridotites as a temperature-dependent partitioning of Fe^{3+}, with increasing incorporation of Fe^{3+} into garnet at higher temperatures. In contrast, the high-temperature stage recorded by our samples shows preferential incorporation of Fe^{3+} into clinopyroxene (Fig. 7d). The subsequent decrease in temperature during equilibration, however, results in a progressive increase of Fe^{3+} in garnet rims and a decrease in clinopyroxenes, indicating a shift of partitioning toward garnet at lower temperatures. This apparent contrast with the trend described for cratonic peridotite and eclogite xenoliths can be explained by the fundamentally different P-T trajectories recorded by our samples. Unlike xenoliths equilibrated along cold, conductive cratonic geotherms, where P and T increase together and Fe^{3+} redistribution may be partly pressure-controlled (Jennings and Holland, 2015), the EL clinopyroxenites record a high-T/P exhumation path from the asthenospheric to the lithospheric mantle. Their strongly decoupled temperature and

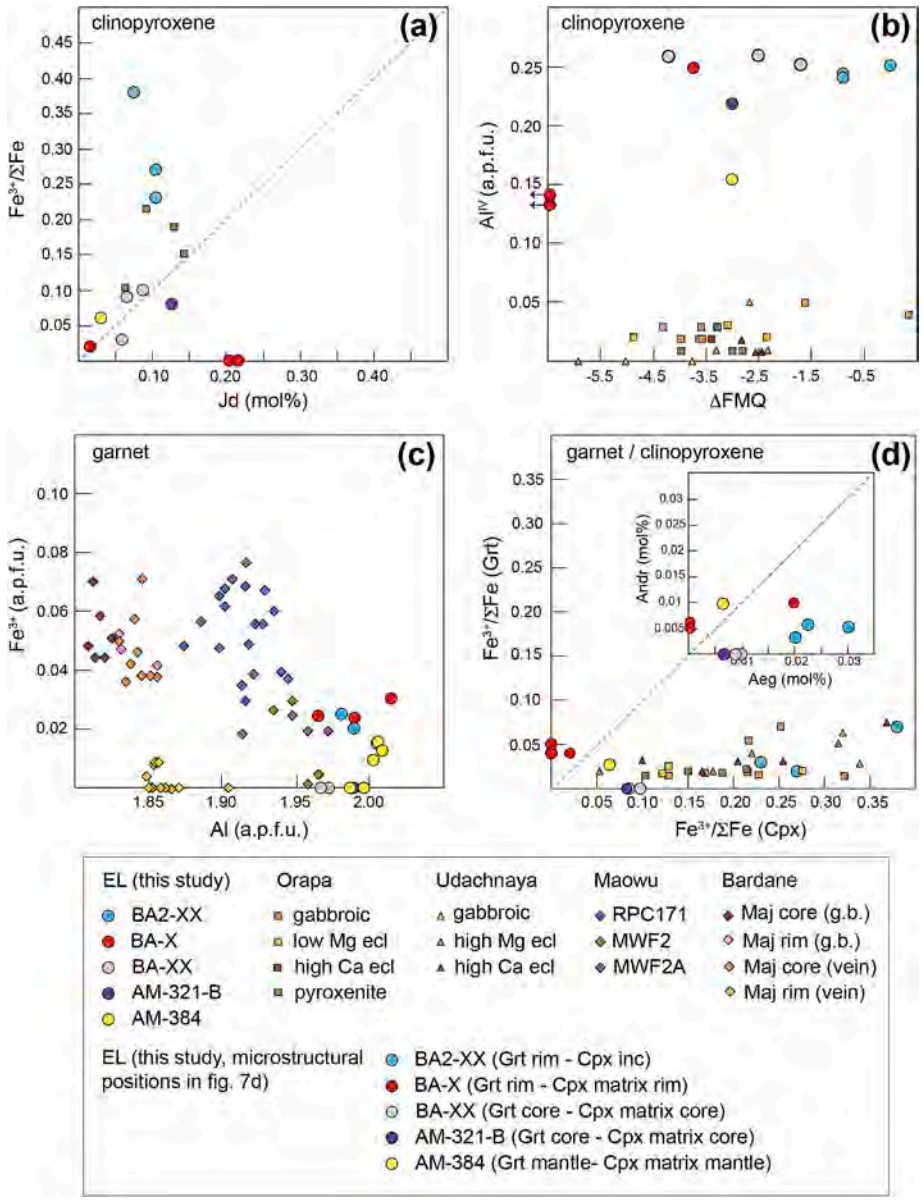

Fig. 7. Variation diagrams of clinopyroxenes (a, b) and garnets (c) of the studied samples. (d) reports $Fe^{3+}/\Sigma Fe$ and the andradite and aegirine components of clinopyroxene/garnet couples at microstructural equilibrium (see text or explanation, Table S1). Our data are compared with clinopyroxenes from subcratonic pyroxenite and eclogite xenoliths from Orapa, Zimbabwe and Udachnaya, Siberia (Aulbach et al., 2020, 2022), and garnets from subduction-related metasomatic garnet-orthopyroxenites from Maowu, China (Malaspina et al., 2017) and websterites from Bardane, Norway (Tumiati and Malaspina, 2019). Abbreviations: EL = External Ligurian, ecl = eclogite, Maj = majoritic garnet, g.b. = grain boundary (see Malaspina et al., 2010 for details about Bardane samples).

pressure evolution results in a Fe^{3+} partitioning trend dominated by cooling at nearly constant pressure, rather than by pressure variations. This resolves the apparent discrepancy with cratonic xenoliths and reflects the contrasting geodynamic environments and equilibration regimes.

4.3. FIB-TEM analyses of clinopyroxene exsolutions

Garnet-facies porphyroclastic clinopyroxene in BA2-XX shows numerous exsolution lamellae with a width of usually less than 1 μm and a spacing of few micrometres. The host clinopyroxene has about 10 mol % Jd and 20 mol% Ca-Ts components with minor Ti. The lamellae appear brighter than the matrix in BSE images with a length of about 10–20 μm (Fig. 2a) but can also look patchy if they are at a low angle to the sample surface. Selected area electron diffraction (Fig. 2c) confirms that the exsolutions are clinoenstatite with space group $P2_1/c$ and a coherent orientation to the clinopyroxene host. The exsolution lamellae are parallel to the (100) plane of clinopyroxene and numerous dislocations are decorating the interface resulting from the lattice mismatch between the two phases. Antiphase domains from the C2/c → $P2_1/c$ displacive transition are well visible in bright field image near zone axis conditions (Fig. 2c). The exsolutions contain no Na and Ti and only very little Ca (~1 mol% Di component). The Al content is still elevated which must be expressed as Mg-Tschermak of about 17 mol% and a small amount of Mg-Eskola component both indicating that the exsolution occurred at still elevated pressures.

5. Discussion and conclusions

5.1. Oxygen fugacity and redox evolution of the studied C-S-bearing clinopyroxenites

The calculation of oxygen fugacity using oxybarometers in mantle pyroxenite samples that do not contain olivine or free SiO_2 is a demanding task. For this reason, we preferred to retrieve the redox state of the studied samples using a forward modelling, exploiting the Fe^{3+} content of clinopyroxenes and garnets in terms of Aeg and Andr components, and assuming a closed system from the crystallisation conditions to the exhumation. This assumption is supported by the preserved

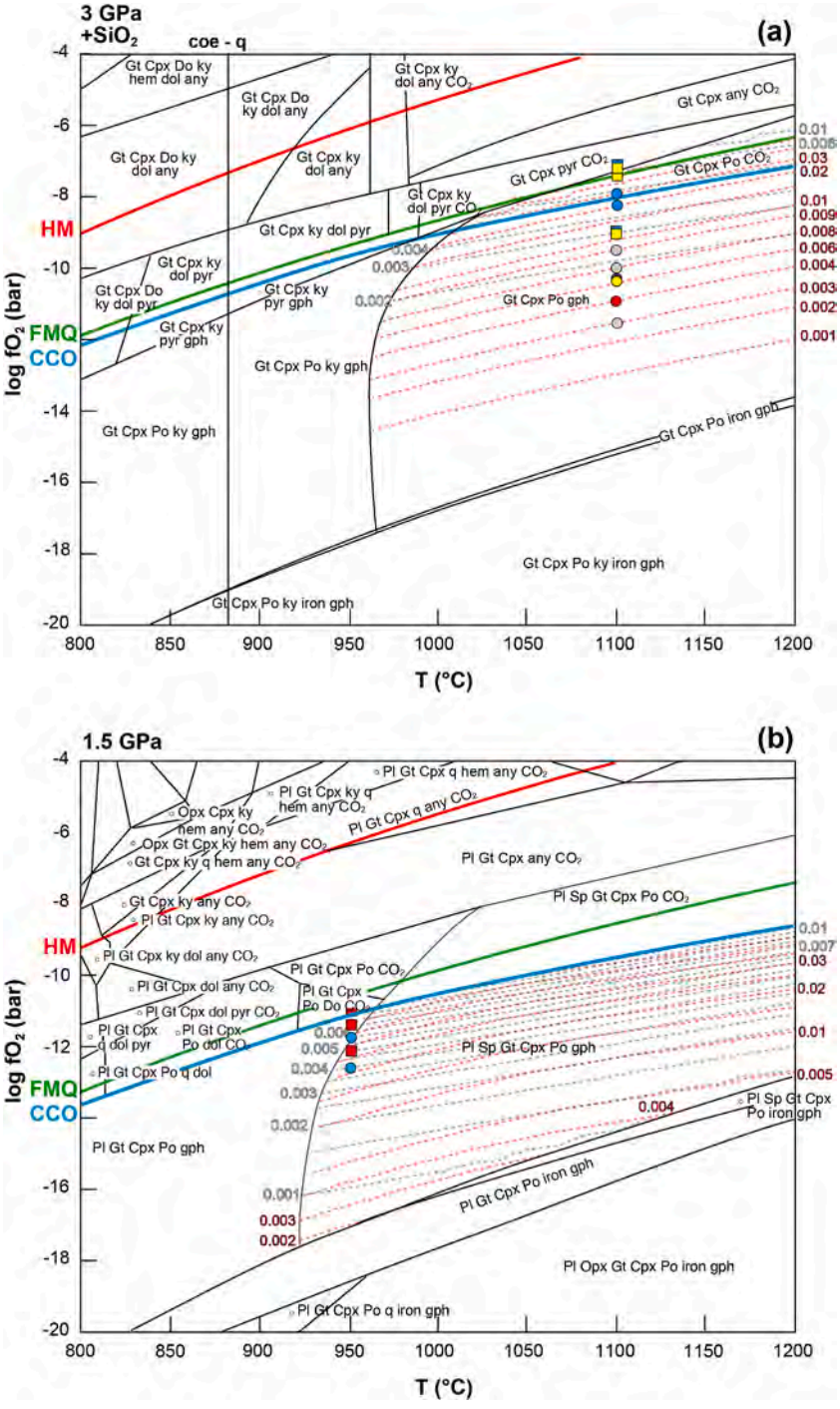

Fig. 8. log fO_2–T section at 3 GPa (a) and 1.5 GPa (b) of pyroxenites BA samples. Grey and red dashed lines (and relative numbers) in the stable phase assemblage area represent isopleths of andradite and aegirine (mol.%), respectively. Note that the model illustrates the subsolidus redox evolution of the solid assemblage. Melt does not appear because the modelled stage corresponds to post-crystallisation cooling under fully solid conditions and at lower dry solidus temperatures. Magnetite is not an equilibrium phase in the rocks but occurs only within sulphide-bearing inclusions. Abbreviations with capital letters refer to abbreviations of solid solution models as reported in the solution_model.dat of Perple_X. Mineral abbreviations: q = quartz, hem = hematite, any = anhydrite, ky = kyanite, dol = dolomite, pyr = pyrite, gph = graphite, coe = coesite. Red, grey and blue curves refer to the hematite-magnetite (HM), fayalite-magnetite-quartz (FMQ) and carbon-CO_2 (CCO) buffers. Garnets (squares) and clinopyroxenes (circles) colours refer to samples as in Fig. 7. (For interpretation of the references to colour in this figure legend, the reader is referred to the web version of this article.)

clinopyroxene-garnet-sulphide assemblage, the lack of secondary alteration or replacement textures, the coherent inclusion-rim microstructures (e.g., clinopyroxene included in garnet cores, exsolution features, etc.), and the presence of graphite at microstructural equilibrium without evidence for external fluid infiltration. Fig. 8 shows two isochemical T-fO_2 sections calculated at 3 and 1.5 GPa. The stable mineral assemblages as shown by microstructures correspond to garnet + clinopyroxene + pyrrhotite + graphite at 3 GPa starting from a T-logfO_2 range of ~970 °C and − 18 bar to ~1025 °C and − 8.25 bar (Fig. 8a), and plagioclase + spinel + garnet (rim) + clinopyroxene + pyrrhotite + graphite at 1.5 GPa starting from a T-logfO_2 range of ~925 °C and − 18 bar to ~960 °C and − 10.5 bar (Fig. 8b). We emphasise that, differently from ultramafic systems (peridotites), the mafic system characteristics of mantle clinopyroxenites may show different pressure-temperature conditions and some overlaps in the stability of garnet, spinel and plagioclase (e.g., Borghini and Fumagalli, 2018). For the sake of simplicity, we did not report the isomodes of the different minerals in the field of interest, considering that the occurrence of spinel and plagioclase is constrained in the kelyphitic microdomains. These field

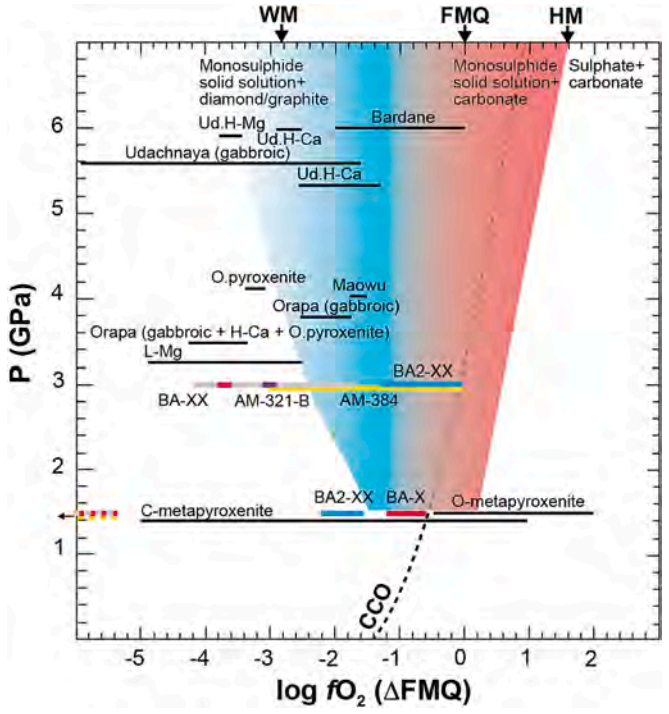

Fig. 9. Ranges values of ΔFMQ = (log fO_2 sample - log fO_2 fayalite-magnetite-quartz buffer) for the studied garnet clinopyroxenites (samples colours refer to Fig. 7) plotted as a function of pressure. They are compared with selected examples of subcratonic pyroxenite and eclogite xenoliths from Orapa and Udachnaya (corrected from Aulbach et al., 2019, 2022 Mikhailenko et al., 2020; Aulbach personal communication), subduction-derived orogenic orthopyroxenites from Maowu (Malaspina et al., 2017) and websterites from Bardane, Norway (Malaspina et al., 2010), and metapyroxenites from continental (Australia, Rio Grande rift, Spitsbergen) and oceanic (Tahiti, Hawaii, Canary Islands) xenoliths (Amundsen and Neumann, 1992). The red-to-blue gradational field represents the fO_2-P space where mantle sulphides and carbonated melt or phases can coexist in a peridotite system, along with the transition between sulphides and sulphates (from Chowdhury and Dasgupta, 2020). Abbreviations: Ud.H-Mg = Udachnaya high Mg eclogites; Ud.H-Ca = Udachnaya high Ca eclogites; H-Ca = Orapa high Ca eclogites; O.pyroxenites = Orapa pyroxenites; L-Mg = Orapa low Mg eclogites; C-metapyroxenite = continental pyroxenite xenoliths; O-metapyroxenite = oceanic pyroxenite xenoliths; WM = wustite-magnetite buffer; HM = hematite-magnetite buffer; CCO = C-CO_2 buffer (calculated at an average temperature of 1000 °C, see Malaspina et al., 2010). (For interpretation of the references to colour in this figure legend, the reader is referred to the web version of this article.)

assemblages are also consistent with equilibration temperatures of 1100 and 950 °C previously calculated by Montanini et al. (2006) and now corrected for the presence of Fe^{3+} in garnets and clinopyroxenes. They are also consistent with the amount of Fe^{3+} measured in clinopyroxenes and garnets in terms of Aeg and Andr mol.% (Fig. 7d), that in Fig. 8 are reported as isopleths in the red and grey dashed lines, respectively. Results are shown with coloured dots (clinopyroxene) and squares (garnet), where colours refer to the same colours of different samples reported in Fig. 7. At 3 GPa the fO_2 values of garnet cores in equilibrium with the included and exsolved matrix clinopyroxenes (Table S1) range from the more oxidised sample BA2-XX with ΔFMQ = −1.25÷0 to the more reduced BA-XX with ΔFMQ = −4.2÷ − 1.6 at 3 GPa (Figs. 8 and 9). At 1.5 GPa the fO_2 values of garnet rims in equilibrium with clinopyroxene rims range from ΔFMQ = −1.2÷ − 0.6 (BA-X) to −2.2÷ − 1.6 (BA2-XX), down to ΔFMQ < −5 for those grains that do not contain Fe^{3+}.

It must be noted that with this approach one should expect an intersection of Aeg and Andr isopleths to retrieve T-fO_2 conditions, where garnet cores, clinopyroxene inclusions and exsolved clinopyroxenes are at equilibrium (same for garnet and clinopyroxene rims). This means that intensive variable (fO_2) and extensive variable (moles of Fe^{3+} in terms of Aeg and Andr components) are in principle considered monotonic functions of the number of moles of O_2 in the system. As already discussed by Evans (2006) and demonstrated by Malaspina et al. (2009, 2012, 2017) and Tumiati and Malaspina (2019) we know very little about the correlation between net bulk oxidation (redox budget) of the system, the fO_2 and the Fe^{3+} partitioning between the mineral phases, the two last ones strongly depending on the temperature and pressure conditions. In fact, at least in eclogite, Fe^{3+} partitioning between garnet and clinopyroxene appears to be itself dependent on fO_2 (see Fig. 6a in Aulbach et al., 2022). The isochemical sections reported in Fig. 8 are not based on a redox equilibrium previously determined from experiments (i.e. oxybarometer) but just report what could be the Fe^{3+} content of clinopyroxene and garnet based on a fixed bulk composition and pressure, at variable temperature and oxygen fugacity. The apparent lack of correlation between Fe^{3+} contents in garnet and clinopyroxene and the calculated fO_2 does not reflect a decoupling from redox conditions. Instead, it results from the redistribution of Fe^{3+} between the two minerals during successive stages of P–T re-equilibration. Because Fe^{3+} partitioning between garnet and clinopyroxene is strongly temperature- and pressure-dependent, the final Fe^{3+} contents primarily record the P–T evolution rather than the absolute fO_2. Even without proper experimental oxybarometers available for these rock compositions and considering all the limitations of forward modelling (minerals thermodynamic database and solid solution models), the results reported in Fig. 8 are consistent with other pyroxenite xenoliths from both lithospheric oceanic and continental mantle, as well as with orogenic metasomatic pyroxenites from the slab-mantle interface (Fig. 9). Also, the occurrence of reduced carbon and sulphur phases agrees with the redox conditions calculated for our samples, as shown by the field where mantle sulphides and carbonates (i.e., oxidised carbon species) can coexist in a peridotite system (Chowdhury and Dasgupta, 2020). Only the most oxidised samples (BA2-XX and AM384) at peak pressure fall in the carbonate/CO_2-sulphide stability (Figs. 8a and 9). This may imply that graphite in our samples could have derived from the reduction of a previous oxidised form of carbon during the retrogression. The microstructure of the coarse flakes of graphite (Fig. 1b) that include those clinopyroxenes recording lower P-T conditions (Fig. 6e) agrees with the hypothesis that its crystallisation occurred during the late stages of equilibration, considering the garnet clinopyroxenite lenses as closed system. Unfortunately, we do not have any petrographic evidence of a previous C^{4+}-bearing phase (carbonate or CO_2-fluid), but we could speculate about the peculiar two-phase inclusions along the decrepitation haloes shown in Figs. 1d and 5b. The clear and transparent portion of the inclusions that does not show any Raman signal could have hosted a CO_2-bearing fluid separated from an earlier sulphide melt, leaked after

the decrepitation occurred during the exhumation, or with such low density that it cannot be detected by Raman spectroscopy. The assumption of the occurrence of an oxidised form of carbon (as immiscible fluids-silicate melt, sulphide melt and supercritical CO_2; e.g., Andersen et al., 1987; Roedder, 1992; Andersen and Neumann, 2001), seems to be confirmed by the occurrence of magnetite in equilibrium with the sulphides included in the garnets (Fig. 5a and c). Indeed, the redox conditions recorded by some garnets and clinopyroxenes of samples BA2-XX and AM384 fall above the FMQ buffer and CCO (Fig. 8a), consistent with the magnetite stability in the inclusions.

5.2. Geodynamic and petrological evolution of the EL clinopyroxenites

The petrological and geochemical work of Montanini et al. (2006) reconstructed the sub-solidus evolution of the EL pyroxenites (and the enclosing peridotites) from 3 GPa and 1100 °C, in the sub-continental lithosphere, to an early decompression stage at 1.5 GPa and 950 °C, possibly related to Late Carboniferous – Early Permian continental extension. The subsequent decompression, including plagioclase-facies shearing occurring at 0.4–0.5 GPa, was likely related to the initiation of the Mesozoic rifting event that led to the formation of the Ligurian-Piedmontese ocean in the Middle Jurassic (Ferrari et al., 2022). During this evolution the studied samples did not experience any fluid/melt rock interaction. Particularly, the occurrence of graphite in the pyroxenites is not related to any external fluid, considering the lack of late-stage fractures or microfractures in the pyroxenite and the absence of carbon- bearing phases in the hosting peridotites. Also, the $\delta^{13}C = -4.3 \div -4.6$ typical of mantle values, along with the high temperature structure of the graphite (Montanini et al., 2010) preclude the possibility of a crystallisation related to late stage, shallow crustal carbon-bearing fluids. The occurrence of Fe-Ni-Cu interstitial sulphides and rounded sulphide blebs included in garnet (Montanini et al., 2010; Fig. 1c, d) are consistent with crystallisation of the garnet clinopyroxenites from sulphur-saturated melts (see also Montanini et al., 2025). The coexistence of pyrrhotite + chalcopyrite + magnetite in the multiphase inclusions derived from sulphide decrepitation (Figs. 1d and 5) may reflect crystallisation from an O-bearing sulphide melt.

The occurrence of clinoenstatite lamellae in the exsolved clinopyroxenes (Fig. 2) could indicate that in the garnet facies stability field the clinopyroxenites crystallised or equilibrated at pressures >3 GPa. Woodland (1998) discussed the stability of a second C2/c pyroxene polymorph in the system Mg-Fe-Si-O at mantle conditions. The clinoenstatite lamellae in the $P2_1/c$ space-group symmetry of our pyroxenes, containing nanometre-scale antiphase domains, could have originally precipitated from a C2/c space-group symmetry pyroxene. However, very little is known about the variation of the P-T conditions of the C2/c to $P2_1/c$ transition when other cations are added in the pyroxene structure, such as Al as in our samples. Indeed, Woodland (1998) demonstrated that the substitution of Fe stabilises the high-P monoclinic polymorph to lower pressure, even if still higher than 3 GPa at 1100 °C. On the other hand, the experimental work of Ulmer and Stalder (2001) did not make any distinction between samples quenched from the high pressure and low pressure clinoenstatite stability fields, precluding the possibility to use exsolution lamellae as geobarometer. The Al content of our clinoenstatite lamellae is expressed as Mg-Tschermak of about 17 mol% and a small amount of Mg-Eskola component, both indicating that the exsolution occurred at still elevated pressures (Knapp et al., 2013). This likely deepens the formation of the EL pyroxenites in the asthenospheric mantle in off-craton environments, usually thinner than cratonic lithospheric mantle (Fig. 10).

Many of the pyroxenites from sub-cratonic mantle xenoliths and those from off-craton orogenic mantle peridotites may be interpreted as derived from (i) redox melting of the mantle, (ii) recycled blocks by delamination of the lower oceanic lithosphere or (iii) deep recycling of an ancient oceanic crust (Foley, 2011). Considering the long-term evolution (1.5 Ga) of the gabbroic protolith of the studied samples, melted after subduction and recycled back by the convective mantle (Montanini et al., 2012, 2025), it is likely that the recycling occurred in the deepest portions of the upper mantle. This crust-derived material may have preserved its redox budget from the time of its detachment from the slab to the crystallisation in the asthenospheric/lithospheric mantle.

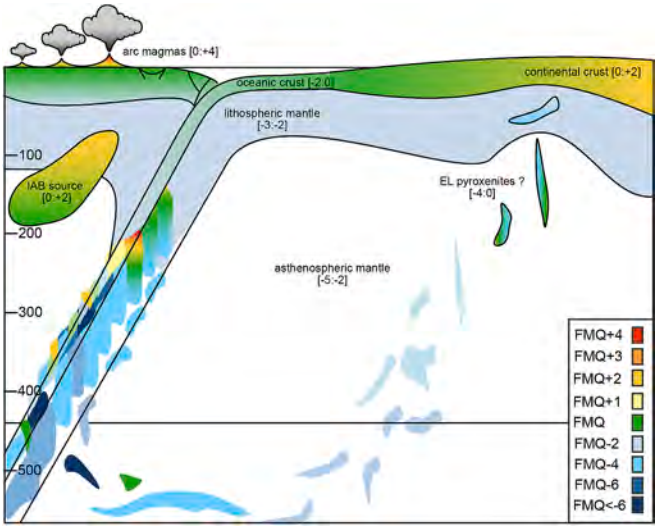

Fig. 10. Schematic cartoon showing various redox conditions of the convective mantle at different depths (km), modified from Foley (2011). Relative proportions are not to scale; numbers in brackets and relative colours in the legend are the values of ΔFMQ. Data are a compilation from Foley (2011) and Cannaò and Malaspina (2018). Abbreviations: IAB = island arc basalts. Note that this sketch is not representative of the regional geological reconstruction of the EL mantle section.

5.3. Decoupling of C—S phases from redox evolution in closed-system recycled crust

The different oxygen fugacity conditions recorded by the convective mantle suggest that its oxidation states vary along short distances and there is significant potential for redox-driven reactions, including melting processes (Foley, 2011). As shown in Fig. 10, while the crust and the upper mantle look homogeneously oxidised and reduced, respectively, subduction zones are strongly heterogeneous in terms of oxygen fugacity, reflecting the different chemical and mineralogical compositions of slab lithologies. Similarly, the asthenospheric mantle far from subduction zones also shows heterogeneities in terms of redox conditions, related to layers of pyroxenites and slab-recycled material, which may have an important role in the element exchange and in the deep recycling of redox-sensitive elements such as carbon and sulphur. Indeed, there is still a strong debate about whether carbon is recycled into the deep mantle in the form of carbonates or diamond, CO_2 or CH_4, and the role that S-bearing phases or fluids may have in its oxidation state. As discussed by Kiseeva et al. (2012), it is widely accepted that at least some carbonate in altered oceanic crust can be stable during subduction and transported deeper into the mantle. Dehydration reactions or partial melting may leave a residue of anhydrous and relatively stable carbonate-bearing eclogite able to be subducted into the deeper upper mantle or even beyond. Poli (2015) experimentally demonstrated that a strongly carbonated gabbro melts at relatively low temperature and pressure (870–900 °C at 120 km of depth), producing a carbonatitic liquid able to metasomatise and oxidise the overlying mantle. At greater depths, recent experimental results indicate that magnesite (magnesite + silicate glass or magnesite + olivine, different from a mafic system) remains stable throughout the mantle but begins to decompose or melt

under specific pressure-temperature conditions (Libon et al., 2024). In particular, magnesite is no longer stable at shallow lower mantle depths (~700 km), where it either melts or reduces to form diamond depending on redox conditions. This suggests that carbonate recycling into the deep mantle may be limited by its reactivity with ambient mantle phases but can be transported at depth if the system is closed.

The stability of carbonates even at very reduced conditions and at pressures and temperatures reaching those of the deep lower mantle has been also demonstrated by Dorfman et al. (2018). They performed experiments on dolomite + iron sandwiches (more similar to a mafic system), where carbon-iron redox interactions destabilised the $MgCO_3$ component, producing a mixture of diamond, Fe_7C_3, and (Mg,Fe)O, but with $CaCO_3$ still preserved. A substantial amount of carbon in the form of tetracarbonates can be incorporated also in silicate melts (ideally a completely melted slab) at the core-mantle boundary, contributing to the polymerisation of silicate melts at those conditions, and favouring the chemical exchange and carbon transport between lower and upper mantle (Cerantola et al., 2023).

The interaction between carbon and sulphur and the role of S-bearing phases in the oxidation or reduction of C-bearing fluids or minerals strongly depend on the geodynamic environment. As discussed by Evans (2012), there is a strong agreement that S^{6+} in anhydrite (reducing to S^{1-} in pyrite, for example) oxidises both Fe and C in lithologies of subduction zones, particularly at high fluid/rock ratios, anhydrite being very soluble in aqueous fluids. Bénard et al. (2018) provided direct evidence for oxidised melts generated at mantle conditions in subduction zones. Their results support the idea that slab-derived oxidised agents, such as sulphates from subducted serpentinites, can migrate through the mantle wedge while maintaining their redox potential, ultimately contributing to the oxidised nature of arc magmas. On the other hand, altered oceanic basalts are already more enriched in hydrothermal pyrite than anhydrite (e.g., Patten et al., 2016) and the fate of sulphur in the form of solid phases will not change its oxidation state during the subduction path. In addition, magmatic sulphides are common accessory minerals in the oceanic crust (Evans et al., 2014). This implies that without fluid/mediated reactions, S and C can in principle keep their stability without interacting, up to very high pressures. Different is the role of Fe-S-O melts when they interact with a C-bearing peridotite. Such melts are able to reduce carbonate into graphite/diamond and dissolve oxygen to allow the reaction (Gunn and Luth, 2006).

Our results suggest that the EL clinopyroxenites derived from a previous sulphide-bearing gabbro that was probably metasomatised at oxidising conditions by C-bearing fluids during subduction. Such a metasomatism could be also responsible of the oxidation of Fe-bearing phases (e.g. clinopyroxene), transforming these rocks into carbonated eclogites that could have preserved their redox budget from subduction up to their melting in the deep mantle. These carbonate/CO_2-bearing, S-saturated silicate melts likely crystallised in the asthenospheric mantle. The segregation of carbonate/CO_2 from the melt at high pressure and more oxidising conditions may have been followed by graphite crystallisation at lower pressures, temperatures, and redox conditions (Fig. 8). Indeed, the ΔFMQ variations recorded by our samples is related to the partitioning of Fe^{3+} in clinopyroxenes due to the temperature decrease from 1100 to 950 °C. Being an intensive variable, the change in fO_2 recorded by different Fe^{3+}/Fe^{2+} ratios in clinopyroxenes and garnets is purely related to a sub-solidus decompression path from the asthenospheric to the lithospheric mantle (Fig. 10). Carbon may be recycled as carbonate phase also at ultrahigh pressures, reducing to diamond or more likely to graphite at lower pressure and temperature conditions without changing the bulk redox conditions of the host system. Overall, our results show that, once crystallised and isolated from fluid–melt interaction, S- and C-bearing recycled lithologies can evolve as effectively closed systems, in which fO_2 variations reflect P–T–dependent Fe^{3+} partitioning rather than redox reactions involving sulphur or carbon. This finding contrasts with the widely held view that sulphur phases play a dominant role in the oxidation state of recycled crust, and thus provides a new perspective on how carbon and sulphur may be transported through the convective mantle without modifying its redox state.

CRediT authorship contribution statement

Nadia Malaspina: Writing – review & editing, Writing – original draft, Visualization, Validation, Methodology, Investigation, Funding acquisition, Conceptualization. **Falko Langenhorst:** Writing – review & editing, Validation, Methodology, Investigation, Funding acquisition, Conceptualization. **Kilian Pollok:** Writing – review & editing, Validation, Methodology, Investigation. **Valerio Cerantola:** Writing – review & editing, Visualization, Validation, Investigation. **Mara Murri:** Writing – review & editing, Investigation, Data curation. **Carolina Longa:** Investigation, Data curation. **Danilo Bersani:** Writing – review & editing, Investigation, Data curation. **Alessandra Montanini:** Writing – review & editing, Supervision, Resources, Conceptualization.

Funding

This work has been financed by the Italian Ministry of University and Research PRIN 2022 "Competing geological and biological processes in underground carbon and hydrogen storage" (Grant n. 20224YR3AZ) and MIUR-DAAD Joint Mobility Program "The redox state of the Earth's mantle: from the slab-mantle interface to the sub-continental lithosphere" (Grant n. 2018-NAZ-0023). N. Malaspina also acknowledges the University of Milano-Bicocca "Redox processes and implications on C-O-H-S budget from the shallow crust to the deep mantle" (Grant n. 2022-ATEQC-0015) and the support of Project MIUR – Dipartimento di Eccellenza 2023–2027 "TECLA" (Grant n. 2023-NAZ-0212). The research also benefited from the equipment and framework of the COMP-HUB and COMP-R Initiatives, funded by the 'Departments of Excellence' program of the Italian Ministry for University and Research (MIUR, 2018–2022 and MUR, 2023–2027).

Declaration of competing interest

The authors declare that they have no known competing financial interests or personal relationships that could have appeared to influence the work reported in this paper.

Acknowledgments

A. Risplendente (University of Milano) is acknowledged for the analytical assistance in electron microprobe. We thank D. Bessas and A. Chumakov for technical assistance during the beamtime at ID18 of ERSF (Grenoble, France). N. Malaspina acknowledges S. Tumiati for discussion of the thermodynamic modelling and O. Müntener for the stimulating scientific exchange.

Appendix A. Supplementary data

Supplementary data to this article can be found online at https://doi.org/10.1016/j.chemgeo.2025.123173.

Data availability

Data are available through Zenodo at http://doi.org/10.5281/zenodo.14685673

References

van Aken, P., Liebscher, B., 2002. Quantification of ferrous/fer- ric ratios in minerals: new evaluation schemes of Fe L_{23} electron energy-loss near-edge spectra. Phys. Chem. Miner. 29, 188–200.

van Aken, P.A., Liebscher, B., Styrsa, V.J., 1998. Quantitative determination of iron oxidation states in minerals using Fe $L_{2,3}$-edge electron energy-loss near-edge structure spectroscopy. Phys. Chem. Miner. 25, 323–327.
Amundsen, H.E.F., Neumann, E.R., 1992. Redox control during mantle/melt interaction. Geochim. Cosmochim. Acta 56, 2405–2416.
Andersen, T., Neumann, E.-R., 2001. Fluid inclusions in mantle xenoliths. Lithos 55, 301–320.
Andersen, T., Griffin, W.L., O'Reilly, S., 1987. Primary sulphide melt inclusions in mantle-derived megacrysts and pyroxenites. Lithos 20, 279–294.
Andrault, D., Muñoz, M., Pesce, G., Cerantola, V., Chumakov, A., Kantor, I., Pascarelli, S., Rüffer, R., Hennet, L., 2017. Large oxygen excess in the primitive mantle could be the source of the Great Oxygenation Event. Geochem. Perspect. Lett. 6, 5–10.
Aulbach, S., Jacob, D.E., 2016. Major- and trace-elements in cratonic mantle eclogites and pyroxenites reveal heterogeneous sources and metamorphic processing of low-pressure protoliths. Lithos 262, 586–605.
Aulbach, S., Smart, K.A., 2023. Petrogenesis and geodynamic significance of xenolithic eclogites. Annu. Rev. Earth Planet. Sci. 51, 521–549.
Aulbach, S., Woodland, A.B., Stern, R.A., Vasilyev, P., Heaman, L.M., Viljoen, K.S., 2019. Evidence for a dominantly reducing Archaean ambient mantle from two redox proxies, and low oxygen fugacity of deeply subducted oceanic crust. Sci. Report. 9, 20190.
Aulbach, S., Viljoen, K.S., Gerdes, A., 2020. Diamondiferous and barren eclogites and pyroxenites from the western Kaapvaal craton record subduction processes and mantle metasomatism, respectively. Lithos 368, 105588.
Aulbach, S., Woodland, A.B., Stagno, V., Korsakov, A.V., Mikhailenko, D., Golovin, A., 2022. Fe3+ distribution and Fe3+/ΣFe-oxygen fugacity variations in kimberlite-borne eclogite xenoliths, with comments on clinopyroxene-garnet oxy-thermobarometry. J. Petrol. 63, egac076.
Aulbach, S., Höfer, H.E., Gerdes, A., Tinguely, C., le Roex, A., 2024. Mélange signatures and low oxygen fugacity in eclogite xenoliths from the crust-mantle transition below a Mesoproterozoic collision belt. J. Geophys. Res. Solid Earth 129, e2023JB027894.
Bénard, A., Klimm, K., Woodland, A.B., Arculus, R.J., Wilke, M., Botcharnikov, R.E., Shimizu, N., Nebel, Ol, Rivard, C., Ionov, D.A., 2018. Oxidising agents in sub-arc mantle melts link slab devolatilisation and arc magmas. Nat. Commun. 9, 3500.
Berly, T.J., Hermann, J., Arculus, R.J., Lapierre, H., 2006. Supra-subduction zone pyroxenites from San Jorge and Santa Isabel (Solomon Islands). J. Petrol. 47, 1531–1555.
Berner, R.A., 2003. The long-term carbon cycle, fossil fuels and atmospheric composition. Nature 426, 323–326.
Bersani, D., Andò, S., Vignola, P., Moltifiori, G., Marino, I.-G., Lottici, P.P., Diella, V., 2009. Spectrochim. Acta Part A Molec. Spectrosc. 73 (3), 484–491.
Borghini, G., Fumagalli, P., 2018. Subsolidus phase relations in a mantle pyroxenite: an experimental study from 0.7 to 1.5 GPa. Eur. J. Mineral. 30, 333–348.
Brandon, A.D., Draper, D.S., 1996. Constraints on the origin of the oxidation state of mantle overlying subduction zones: an example from Simcoe, Washington, USA. Geochim. Cosmochim. Acta 60, 1739–1749.
Canil, D., O'Neill, H.S.C., 1996. Distribution of ferric iron in some upper-mantle assemblages. J. Petrol. 37, 609–635.
Canil, D., O'Neill, H.S.C., Pearson, D.G., Rudnick, W.F., McDonough, D.A., Carswell, D., 1994. Ferric iron in peridotites and mantle oxidation states. Earth Planet. Sci. Lett. 123, 205–220.
Cannaò, E., Malaspina, N., 2018. From oceanic to continental subduction: Implications for the geochemical and redox evolution of the supra-subduction mantle. Geosphere 14, 2311–2336.
van Cappellen, E.V., Doukhan, J.C., 1994. Quantitative transmission X-ray micro-analysis of ionic compounds. Ultramicroscopy 53, 343–349.
Cerantola, V., Sahle, C.J., Petitgirard, S., Wu, M., Checchia, S., Weis, C., Di Michiel, M., Vaughan, G.B.M., Collings, I.E., Arató, E., Wilke, M., Jones, A.P., Hanfland, M., Tse, J.S., 2023. Tetracarbonates in silicate melts may be at the origin of a deep carbon reservoir in the deep Earth. Commun. Earth Environ. 4, 67.
Chowdhury, P., Dasgupta, R., 2020. Sulfur extraction via carbonated melts from sulfide-bearing mantle lithologies – Implications for deep sulfur cycle and mantle redox. Geochim. Cosmochim. Acta 269, 376–397.
Connolly, J.A., 2005. Computation of phase equilibria by linear programming: a tool for geodynamic modeling and its application to subduction zone decarbonation. Earth Planet. Sci. Lett. 236, 524–541.
Davies, G.R., Nixon, P.H., Pearson, D.G., Obata, M., 1993. Tectonic implications of graphitized diamonds from the Ronda peridotite massif, southern Spain. Geology 21, 471–474.
Dorfman, S., Badro, J., Nabiei, F., Prapenka, V.B., Cantoni, M., Gillet, P., 2018. Carbonate stability in the reduced lower mantle. Earth Planet. Sci. Lett. 489, 84–91.
Evans, K.A., 2006. Redox decoupling and redox budgets: Conceptual tools for the study of earth systems. Geology 34, 489–492.
Evans, K.A., 2012. The redox budget of subduction zones. Earth Sci. Rev. 113, 11–32.
Evans, K.A., Tomkins, A.G., Cliff, J., Fiorentini, M.L., 2014. Insights into subduction zone sulfur recycling from isotopic analysis of eclogite-hosted sulfides. Chem. Geol. 365, 1–19.
Ferrari, E., Montanini, A., Tribuzio, R., 2022. Rifting evolution of the lithospheric subcontinental mantle: New insights from the External Ligurian ophiolites (Northern Apennine, Italy). Lithos 410-411, 106571.
Foley, S., 2011. A Reappraisal of Redox Melting in the Earth's Mantle as a Function of Tectonic setting and Time. J. Petrol. 52, 1363–1391.
Franzolin, E., Schmidt, M.W., Poli, S., 2011. Ternary Ca–Mg–Fe carbonates: subsolidus phase relations at 3.5 GPa and a thermodynamic solid solution model including order/disorder. Contrib. Mineral. Petrol. 161, 213–227.
Frost, D.J., Langenhorst, F., 2002. The effect of Al2O3 on Fe- Mg partitioning between magnesiowustite and magnesium silicate perovskite. Earth Planet. Sci. Lett. 199, 227–241.
Green, E.C.R., White, R.W., Diener, J.F.A., Powell, R., Holland, T.J.B., Palin, R.M., 2016. Activity–composition relations for the calculation of partial melting equilibria for metabasic rocks. J. Metamorph. Geol. 34, 845–869.
Gunn, S.C., Luth, R.W., 2006. Carbonate reduction by Fe-S-O melts at high pressure and high temperature. Am. Mineral. 91, 1110–1116.
Hanger, B.J., Yaxley, G.M., Berry, A.J., Kamenetsky, V.S., 2015. Relationships between oxygen fugacity and metasomatism in the Kaapvaal subcratonic mantle, represented by garnet peridotite xenoliths in the Wesselton kimberlite, South Africa. Lithos 212–215, 443–452.
Hirschmann, M.M., 2018. Comparative deep Earth volatile cycles: the case for C recycling from exosphere/mantle fractionation of major (H2O, C, N) volatiles and from H2O/Ce, CO2/Ba, and CO2/Nb exosphere ratios. Earth Planet. Sci. Lett. 502, 262–273.
Holland, T.J.B., Powell, R., 1998. An internally consistent thermodynamic data set for phases of petrological interest. J. Metamorph. Geol. 16, 309–343.
Holland, T.J.B., Powell, R., 2003. Activity–composition relations for phases in petrological calculations: an asymmetric multicomponent formulation. Contrib. Mineral. Petrol. 145, 492–501.
Holland, T.J.B., Powell, R., 2011. An improved and extended internally consistent thermodynamic dataset for phases of petrological interest, involving a new equation of state for solids. J. Metamorph. Geol. 29, 333–383.
Holland, T.J.B., Green, E.C., Powell, R., 2018. Melting of peridotites through to granites: a simple thermodynamic model in the system KNCFMASHTOCr. J. Petrol. 59, 881–900.
Jennings, E.S., Holland, T.J.B., 2015. A simple Thermodynamic Model for Melting of Peridotite in the System NCFMASOCr. J. Petrol. 56, 869–892.
Kiseeva, E.S., Yaxley, G.M., Hermann, J., Litasov, K.D., Rosenthal, A., Kamenetsky, V.S., 2012. An experimental study of carbonated eclogite at 3.5-5.5 GPa - Implications for silicate and carbonate metasomatism in the cratonic mantle. J. Petrol. 53, 727–759.
Knapp, N., Woodland, A.B., Klimm, K., 2013. Experimental constraints in the CMAS system on the Ca-Eskola content of eclogitic clinopyroxene. Eur. J. Mineral. 25, 579–596.
Kopylova, M.G., Russell, J.K., Cookenboo, H., 1999. Petrology of Peridotite and Pyroxenite Xenoliths from the Jericho Kimberlite: Implications for the thermal State of the Mantle beneath the Slave Craton, Northern Canada. J. Petrol. 40, 79–104.
Kornprobst, J., Piboule, M., Roden, M., Tabit, A., 1990. Corundum-bearing garnet clinopyroxenites at Beni Bousera, Morocco: original plagioclase-rich gabbros recrystallized at depth within the mantle? J. Petrol. 31, 717–745.
Langenhorst, F., Joreau, P., Doukhan, J.C., 1995. Thermal and shock metamorphism of the Tenham chondrite: a TEM examination. Geochim. Coscmochim. Acta 59, 1835–1845.
Libon, L., Spiekermann, G., Blanchard, I., Kaa, J.M., Dominijanni, S., Sieber, M.J., Forster, M., Albers, C., Morgenroth, W., McCammon, C., Schreiber, A., Roddatis, V., Glazyrin, K., Husband, R.J., Hennet, L., Appel, K., Wilke, M., 2024. Reevaluating the fate of subducted magnesite in the Earth's lower mantle. Phys. Earth Planet. Inter. 355, 107238.
Malaspina, N., Poli, S., Fumagalli, P., 2009. The oxidation state of metasomatized mantle wedge: insights from C–O–H-bearing garnet peridotite. J. Petrol. 50, 1533–1552.
Malaspina, N., Scambelluri, M., Poli, S., Van Roermund, H.L.M., Langenhorst, F., 2010. The oxidation state of mantle wedge majoritic garnet websterites metasomatised by C-bearing sub- duction fluids. Earth Planet. Sci. Lett. 298, 417–426.
Malaspina, N., Langenhorst, F., Fumagalli, P., Tumiati, S., Poli, S., 2012. Fe^{3+} distribution between garnet and pyroxenes in mantle wedge carbonate-bearing garnet peridotites (Sulu, China) and implications for their oxidation state. Lithos 146–147, 11–17.
Malaspina, N., Langenhorst, F., Tumiati, S., Campione, M., Frezzotti, M.L., Poli, S., 2017. The redox budget of crust-derived fluid phases at the slab-mantle interface. Geochim. Cosmochim. Acta 209, 70–84.
Malaspina, N., Borghini, G., Zanchetta, S., Pellegrino, L., Corti, M., Tumiati, S., 2023. Geochemical evolution of melt/peridotite interaction at high pressure in subduction zones. Geochem. Perspect. Lett. 24, 48–52.
Manatschal, G., Müntener, O., 2009. A type sequence across an ancient magma- poor ocean–continent transition: the example of the western Alpine Tethys ophiolites. Tectonophysics 473, 4–19.
Marchesi, C., Garrido, C.J., Bosch, D., Bodinier, J.L., Gervilla, F., Hidas, K., 2013. Mantle refertilization by melts of crustal-derived garnet pyroxenite: evidence from the Ronda peridotite massif, southern Spain. Earth Planet. Sci. Lett. 362, 66–75.
Marroni, M., Molli, G., Montanini, A., Ottria, G., Pandolfi, L., Tribuzio, R., 2002. The External Ligurian units (Northern Appennine, Italy): from rifting to convergence of a fossil ocean-transition zone. Ofioliti 27 (2), 119–131.
Marroni, M., Meneghini, F., Pandolfi, L., 2017. A revised subduction inception model to explain the late cretaceous, double-vergent orogen in the precollisional western tethys: evidence from the Northern Apennines. Tectonics 36, 2227–1149.
Mikhailenko, D.S., Stagno, V., Korsakov, A.V., Andreozzi, G.B., Marras, G., Cerantola, V., Malygina, E.V., 2020. Redox state determination of eclogite xenoliths from Udachnaya kimberlite pipe (Siberian craton), with some implications for the graphite/diamond formation. Contrib. Mineral. Petrol. 175, 107.
Montanini, A., Tribuzio, R., 2015. Evolution of recycled crust within the mantle: Constraints from the garnet pyroxenites of the External Ligurian ophiolites (northern Apennines, Italy). Geology 43, 911–914.
Montanini, A., Tribuzio, R., Anczkiewicz, R., 2006. Exhumation history of a garnet pyroxenite-bearing mantle section from a continent–ocean transition, Northern Apennine ophiolites, Italy. J. Petrol. 47, 1943–1971.

Montanini, A., Tribuzio, R., Bersani, D., 2010. Insights into the origin of mantle graphite and sulphides in garnet pyroxenites from the External Liguride peridotites, Northern Apennine, Italy. In: Coltorti, M., Downes, H., Gregoire, M., O'Reilly, S.Y. (Eds.), Petrological Evolution of the European Lithospheric Mantle, vol. 337. Geological Society of London Special Publication, pp. 87–105.

Montanini, A., Tribuzio, R., Thirlwall, M., 2012. Garnet clinopyroxenite layers from the mantle sequences of the Northern Apennine ophiolites (Italy): evidence for recycling of crustal material. Earth Planet. Sci. Lett. 351-352, 171–181.

Montanini, A., Luguet, A., van Acken, D., Tribuzio, R., Schuth, S., Nowell, G.M., 2025. From crustal protoliths to mantle garnet pyroxenites: insights from Os isotopes and highly siderophile elements. Geochim. Cosmochim. Acta 402, 217–233.

Müntener, O., Pettke, T., Desmurs, L., Meier, M., Schaltegger, U., 2004. Refertilization of mantle peridotite in embryonic ocean basins: trace element and Nd- isotopic evidence and implications for crust–mantle relationships. Earth Planet. Sci. Lett. 221, 293–308.

Notini, L., Scambelluri, M., Tommasi, A., Tommasi, A., Ferri, F., Rodríguez-Vargas, A., Rampone, E., 2024. Probing the deep mantle wedge in an active subduction zone: Xenoliths from the Mercaderes Volcanic District, Southern Colombia. Lithos 464-465, 107401.

Palyanov, Y.N., Borzdov, Y.M., Bataleva, Y.V., Sokol, A.G., Palyanova, G.A., Kupriyanov, I.N., 2007. Reducing role of sulfides and diamond formation in the Earth's mantle. Earth Planet. Sci. Lett. 260, 242–256.

Patten, C.G.C., Pitcairn, I.K., Teagle, D.A.H., Harris, M., 2016. Sulphide mineral evolution and metal mobility during alteration of the oceanic crust: Insights from ODP Hole 1256D. Geochim. Cosmochim. Acta 193, 132–159.

Pearson, D.G., Nowell, G.M., 2004. Re–Os and Lu–Hf isotope constraints on the origin and age of pyroxenites from the Beni Bousera Peridotite Massif: implications for mixed peridotite–pyroxenite mantle sources. J. Petrol. 45, 439–455.

Pearson, D.G., Davies, G.R., Nixon, P.H., 1993. Geochemical Constraints on the Petrogenesis of Diamond Facies Pyroxenites from the Beni Bousera Peridotite Massif, North Morocco. J. Petrol. 34, 125–172.

Pellegrino, L., Malaspina, N., Zanchetta, S., Langone, A., Tumiati, S., 2020. High pressure melting of eclogites and metasomatism of garnet peridotites from Monte Duria Area (Central Alps, N Italy): a proxy for melt-rock reaction during subduction. Lithos 358–359, 10539.

Pellegrino, L., Menegon, L., Zanchetta, S., Langenhorst, F., Pollok, K., Tumiati, S., Malaspina, N., 2021. Reaction-induced mantle weakening at high-pressure conditions: an example from garnet pyroxenites of Ulten Zone (Eastern Alps, N Italy). J. Gephys. Res.: Solid Earth 126, e2021JB022584.

Piccardo, G.B., 2008. The Jurassic Ligurian Tethys, a fossil ultraslow-spreading ocean: The mantle perspective. In: Coltorti, M., Gregoire, M. (Eds.), Metasomatism in Oceanic and Continental Lithospheric Mantle, 293. Geological Society of London Special Publication, pp. 11–33.

Poli, S., 2015. Carbon mobilized at shallow depths in subduction zones by carbonatitic liquids. Nat. Geosci. 8 (633), 636.

Potapkin, V., Chumakov, A.I., Smirnov, G.V., Celse, J.P., Ruffer, R., McCammon, C., Dubrovinsky, L., 2012. The ^{57}Fe Synchrotron Mössbauer Source at the ESRF. J. Synchrotron Radiat. 19, 559–569.

Powell, R., Holland, T.J.B., 1999. Relating formulations of the thermodynamics of mineral solid solutions; activity modeling of pyroxenes, amphiboles, and micas. Am. Mineral. 84 (1–2), 1–14.

Rampone, E., Hoffmann, A.W., Piccardo, G.B., Vannucci, R., Bottazzi, P., Ottolini, L., 1995. Petrology, mineral and isotope geochemistry of the External Liguride peridotites, northern Apennine, Italy. J. Petrol. 36, 81–105.

Rampone, E., Piccardo, G.B., Hofmann, A.W., 2008. Multistage melt–rock interaction in the Mt. Maggiore (Corsica, France) ophiolitic peridotites: microstructural and geochemical records. Contrib. Mineral. Petrol. 156, 453–475.

Rielli, A., Tomkins, A.G., Nebel, O., Brugger, J., Etschmann, B., Zhong, R., Yaxley, G.M., Paterson, D., 2017. Evidence of sub-arc mantle oxidation by Sulphur and carbon. Geochem. Perspect. Lett. 124–132.

Roedder, E., 1992. Fluid inclusion evidence for immiscibility in magmatic differentiation. Geochim. Cosmochim. Acta 56, 5–20.

Simakov, S.K., 1998. Redox state of Earth' s upper mantle peridotites under the ancient cratons and its connection with diamond genesis. Geochim. Cosmochim. Acta 62, 1811–1820.

Tribuzio, R., Thirlwall, M., Vannucci, R., 2004. Origin of the gabbro-peridotite association form the Northern Apennine ophiolites (Italy). J. Petrol. 45, 1109–1124.

Tumiati, S., Malaspina, N., 2019. Redox processes and the role of carbon-bearing volatiles from the slab–mantle interface to the mantle wedge. J. Geol. Soc. Lond. 176, 388–397.

Ulmer, P., Stalder, R., 2001. The Mg(Fe)SiO3 orthoenstatite-clinoenstatite transitions at high pressures and temperatures determined by Raman-spectroscopy on quenched samples. Am. Mineral. 86, 1267–1274.

Wang, J., Hattori, K.H., Stern, C.R., 2008. Metasomatic origin of garnet orthopyroxenites in the subcontinental lithospheric mantle underlying Pali Aike volcanic field, southern South America. Mineral. Petrol. 94 (3–4), 243–258.

Wood, B.J., Bryndzia, L.T., Johnson, K.E., 1990. Mantle oxidation state and its relationship to tectonic oxidation and its relationship to tectonic environment and fluid speciation. Science 248, 337–345.

Woodland, A.B., 1998. The orthorhombic to high-P monoclinic phase transition in Mg-Fe pyroxenes: can it produce a seismic discontinuity? Geophys. Rres. Lett. 25, 1241–1244.

Woodland, A.B., 2009. Ferric iron contents of clinopyroxene from cratonic mantle and partitioning behaviour with garnet. Lithos 112, 1143–1149.

Woodland, A.B., Kornprobst, J., Tabit, A., 2006. Ferric iron in orogenic lherzolite massifs and controls of oxygen fugacity in the upper mantle. Lithos 89, 222–241.

Yaroslavtsev, S., 2023. SYNCmoss software package for fitting Mössbauer spectra measured with a synchrotron Mössbauer source. J. Synchrotron Radiat. 30, 596–604.

Yaxley, G.M., Berry, A.J., Kamenetsky, V.S., Woodland, A.B., Golovin, A.V., 2012. An oxygen fugacity profile through the Siberian Craton—Fe K-edge XANES determinations of $Fe^{3+}/\Sigma Fe$ in garnets in peridotite xenoliths from the Udachnaya East kimberlite. Lithos 140–141, 142–151.